European Polymer Journal 216 (2024) 113280

Contents lists available at ScienceDirect

European Polymer Journal

journal homepage: www.elsevier.com/locate/europolj

Developing multifunctional pectin-based hydrogel for wound dressing: *In silico, in vitro* and *in vivo* evaluation

Banu Kocaağa [a,*], Yetkin Öztürk [b], H. Ceren Kurçin [a], Ö. Zeynep Güner-Yılmaz [a], Ozge Kurkcuoglu [a], Melkon Tatlier [a], İlkay Özdemir [c], Elif Kervancioglu Demirci [c], Tuğba Kotil [c], Seyhun Solakoğlu [c], Burak Aksu [d], Saime Batirel [e], Ayça Bal-Öztürk [f,g,h], F. Seniha Güner [a,i]

[a] *Department of Chemical Engineering, Istanbul Technical University, Maslak, Istanbul 34469, Turkey*
[b] *Department of Molecular Biology and Genetics, Istanbul Technical University, Maslak, Istanbul 34469, Turkey*
[c] *Department of Histology and Embryology, Istanbul Faculty of Medicine, Istanbul University, Istanbul 34093, Turkey*
[d] *Department of Medical Microbiology, School of Medicine, Marmara University, Istanbul 34854, Turkey*
[e] *Department of Medical Biochemistry, School of Medicine, Marmara University, Istanbul 34854, Turkey*
[f] *Faculty of Pharmacy, Istinye University, Zeytinburnu, 34010 Istanbul, Turkey*
[g] *Stem Cell and Tissue Engineering R&D Center, Istinye University, 34010 Istanbul, Turkey*
[h] *Institute of Health Sciences, Department of Stem Cell and Tissue Engineering, Istinye University, 34010 Istanbul, Turkey*
[i] *Sabancı University Nanotechnology Research and Application Center (SUNUM), 34956 Istanbul, Turkey*

ARTICLE INFO

Keywords:
Pectin
Wound healing
Zeolite
Molecular dynamics

ABSTRACT

Multifunctional hydrogel wound dressing with high hemostatic, antioxidant, and self-healing activity is desirable in clinical applications. In this contribution, we developed two distinct hydrogel formulations, namely PZ and PTBA, by employing low methoxyl pectin (P), zeolite, or 2-thiobarbituric acid (TBA) for sustained release of procaine (PC) in a controlled manner up to 40 h. These hydrogel systems (PZ and PTBA) utilize dynamic reversible hydrogen bonds between the components and a metal coordination bond between carboxyl acid groups of pectin chains and Ca^{2+} to confer self-healing properties, as demonstrated by molecular dynamics (MD) and rheological analyses. Moreover, PZ and PTBA hydrogels possess superior antioxidant, hemostasis, biocompatibility, and antibacterial activities. The data from the mouse skin incision model and infected full-thickness skin wound model demonstrated the highest wound closure rate (wound closure area per day) was achieved by the PZ (4.72) and PTBA (4.62) groups on day 21, which was better than the control (4.2) and Kaltostat groups (4.05) ($p < 0.05$). PZ and PTBA's effectiveness in wound closure and acceleration of the wound healing process, highlighting its significant potential in wound management.

1. Introduction

Wound healing is a dynamic, ordered sequential process that requires various chemical, biochemical, and cellular processes to perform tissue repair and regeneration. Today, the growing need for effective wound care products is driven by several factors, including the rising prevalence of chronic wounds, the growing elderly population, the increasing number of surgical procedures, and the global incidence of accidents such as road accidents, burns, and traumas, global disasters and military interventions [1].

Wound dressings have always been considered essential devices in wound healing management. Traditional wound dressings serve as a physical barrier but does not significantly contribute to the reconstruction of damaged tissue. Advanced wound dressings, on the other hand, are expected not only provide a physical barrier but also enhance the healing process; they have mechanical durability, long shelf life, and cost-effectiveness [2–4]. Furthermore, rapid and effective hemostasis is very crucial to improve patient survival, particularly in the case of emergency medical treatment [5,6]. However, many of the advanced wound dressings available in the market fall short of meeting all these requirements. With this motive, various biomaterials have been developed using different chemicals in different forms, such as modified gauze, bandages, foams, sponges, films, hydrogels, and 3-dimensional (3D) scaffolds similar to the extracellular matrix (ECM) [4,7].

* Corresponding author.
E-mail address: bkocaaga@itu.edu.tr (B. Kocaağa).

https://doi.org/10.1016/j.eurpolymj.2024.113280
Received 14 February 2024; Received in revised form 27 June 2024; Accepted 30 June 2024
Available online 1 July 2024

Among these, pectin-based hydrogels have been shown to collect numerous features desirable for an advanced wound dressing. These include biocompatibility [8,9], antibacterial [10], hemostatic [11], antioxidant [12], self-healing [13–15], bioadhesion [8], biodegradability [16], oxygen permeability [17], availability and renewability properties [18].

By utilizing pectin's intrinsic antibacterial activity, antibiotic-resistant bacteria can be avoided. Pectin can provide sustained antimicrobial protection attributed to its unique structural features and functional groups while minimizing tissue damage [10,19]. Additionally, pectin, a plant polysaccharide, possesses remarkable antioxidant capabilities and can modulate the overproduction of reactive oxygen species (ROS), which can impair wound healing. The scavenging ability of pectin hydrogel can reduce the levels of ROS generated during oxidative stress [20–22]. Furthermore, the self-healing capability of pectin hydrogel allows it to adapt and withstand body movement, extending the life of the dressing and avoiding the re-opening of wounds, which can cause infection and delay healing. Injectable pectin hydrogel can fill irregular wounds of different shapes and depths [15,23]. Therefore, pectin hydrogels promise to respond to the immediate need for a wound dressing that can serve multiple functions.

Here, we developed two new hydrogel films based on low-methoxy pectin. These films are characterized by their pH-sensitivity, dual cross-linking structure, capability to administer drugs, and facilitation of wound healing. The weak mechanical properties of the pectin hydrogel films are significantly enhanced through the incorporation of either zeolite-A or 2-thiobarbituric acid (TBA). Zeolitic frameworks are composed of TO_4 tetrahedra $[SiO_4]4-$ and $[AlO_4]5-$ interconnected by oxygen atoms [24], emerge as an outstanding candidate in tissue engineering. This is attributed to its varied and intricate pore sizes, three-dimensional structures, biocompatibility, non-toxic nature, and antibacterial qualities [25–28]. Zeolites promote wound healing through cell adhesion via silanol groups and by stimulating cell proliferation [29]. They also demonstrate remarkable hemostatic abilities, efficiently adsorbing high concentrations of clotting factors and platelets [30–33]. Recent studies further highlight their antioxidant capabilities. [34,35]. The integration of zeolite into the pectin matrix not only augments the mechanical properties but also enhances the biomedical potential of the wound dressing network. [17,36]. Our prior *in vitro* investigations on multiple zeolites, including zeolite A, revealed that their crystallinity remains unaltered in Simulated Body Fluid (SBF), without any deleterious effects on cultured cells. Zeolites exhibit inert behavior in such environments, with no degradation impeding cell development. Concurrently, recent *in vivo* studies indicate that zeolite A is biocompatible with bone tissues, fostering normal development without inducing necrosis or adverse reactions [37,38].

TBA, on the other hand, is recognized for its antioxidant, antifungal, antidiabetic, and anti-cancer properties, and it promotes a conducive environment for cell adhesion [39,40]. We have previously enhanced the pectin matrix by physically functionalizing it with thiol groups via TBA incorporation, resulting in an extended degradation timeframe and improved biocompatibility [41].

Local anesthetics (LAs), known for their effective analgesic properties through voltage-gated sodium channel blockade, also exhibit antimicrobial and antifungal properties. One particular local anesthetic (LA), procaine hydrochloride (PC), has multiple benefits, including applications in chemotherapy, modulating cell membranes, antioxidant activity, increasing resistance to infection and toxins, and promoting neuron regeneration [42–48]. PC is particularly effective in treating burn wounds and is used as both a pain reliever and long-term survival aid during oncological surgery [48–52].

In this research, we conducted a comparative analysis of the wound healing efficacies of Pectin-Zeolite (PZ) and Pectin-TBA (PTBA) hydrogel films against Kaltostat®, a commercially prevalent alginate-based dressing [84,85]. Kaltostat® is recognized for its chiral structure and is extensively employed in the management of diverse wound types [86], including pressure [87], diabetic foot [88], and acute carotid endarterectomy wounds [89]. Moreover, Kaltostat® has been identified as a superior alternative to hydrofiber dressings in the context of wound healing, particularly notable in pediatric care [90].

We first conducted Molecular Dynamics (MD) simulations in explicit water to better understand the dynamic cross-linking behavior that can give zeolite- and TBA-added films self-healing properties and structural stiffening, which improves wound dressing stability and drug release profile. We then analyze the conformational, morphological, and structural properties of the synthesized hydrogels using scanning electron microscopy (SEM), differential scanning calorimetry (DSC), contact angle measurements, rheology, swelling, and drug release analysis. Further *in vitro* studies revealed the self-healing ability, moldable qualities, biocompatibility, antibacterial, antioxidant, and hemostatic properties of the pectin-based hydrogels with zeolite (PZ) or TBA (PTBA). Finally, the efficacy of PZ and PTBA hydrogels in wound healing was evaluated in Sprague Dawley rats and compared with the positive control group using Kaltostat® dressing. The results of the study were confirmed through histological examination of the skin.

2. Results and discussion

2.1. Molecular dynamic simulations of polygalacturonic acid, TBA, and PC systems

We performed all-atom MD simulations in explicit water for two different systems of polygalacturonic acid (PGAL): (i) with TBA (called TGAL) (Fig. S1a) and (ii) with TBA and procain (PC) (Fig. S1b) (called PTGAL) to understand the cross-linking behavior of the polymeric chains promoting self-healing and dynamic stability. Simulation details are listed in Table 1.

Each independent 200 ns MD simulation in two replicas were checked for equilibrium by monitoring the energy deviation and root mean squared deviation (RMSD) profiles. Graphs displaying both electrostatic and van der Waals energies for the TGAL and PTGAL models were illustrated in Fig. S2.

RMSD, Radius of gyration (Rg), and End-to-end distance (Rn) calculations give an idea about the globular motions and overall flexibility of the polymer chains. Therefore, the dynamics of models were evaluated for each system for each independent run, using RMSD, Rg and Rn distributions, which are illustrated in Fig. 1a, c, e as violin graph; and as a function of time in Fig. 1b, d and f, respectively. RMSD of cross-linked chains was calculated using the conformations at $t = 0$ ns as a reference to measure its structural deviations. The PGAL chains showed relatively high RMSD values of 10–15 Å, indicating that they deviated from their initial conformations. These deviations can be attributed to the notable flexibility and compactness of the cross-linked PGAL chains in the TBA and TBA-PC solutions. This behavior is further supported by the observed changes in the radius of gyration (Rg) and the end-to-end distance (Rn), with median values of 17.7 and 18.1 for TGAL and PTGAL, respectively, for Rg, and 48.4 and 46.2, respectively, for Rn (as

Table 1
Details of the systems investigated in this study.

Code	Number of TBA molecules per box	Number of procaine molecules per box	Number of PGAL chains	Number of cross-linker Ca2 + ions	Simulation length (ns)
TGAL	5	–	2	20	200 × 2
TGAL-II	5	–	2	20	200 × 2
PTGAL-I	5	5	2	20	200 × 2
PTGAL-II	5	5	2	20	200 × 2

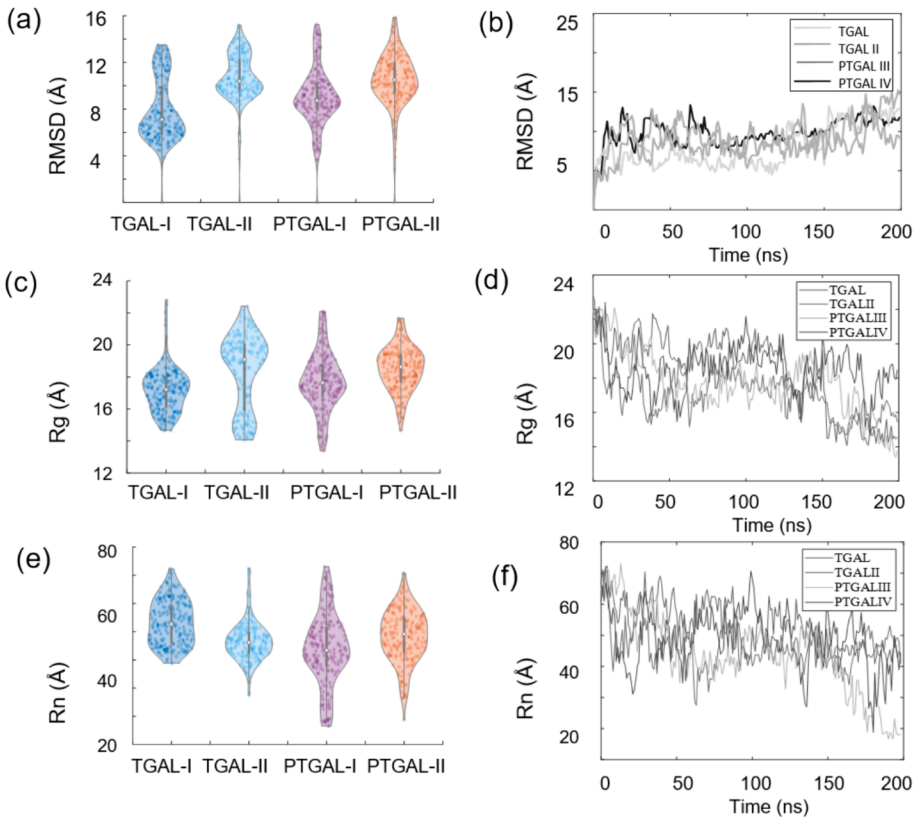

Fig. 1. Dynamics of cross-linked PGAL chains for TGAL and PTGAL models. Violin plots for (a) RMSD, (b) Rg, (e) Rn; plots as a function of time for (b) RMSD, (d) Rg, (f) Rn are displayed for independent run of each system.

shown in Fig. 1c-f and Table S1). Although the PGAL chains can establish dynamic dual secondary bonds through cross-linking, their flexibility appears to be the primary factor contributing to their high RMSD values with median values of of 9.6 and 9.8 for TGAL and PTGAL, respectively, (Fig. 1c-f, Table S1). Furthermore, the Wilcoxson rank sum test was employed to compare the Rg and Rn distributions of TGAL and PTGAL models (Table S2). The test results showed that the *p*-values of 1.28 x 10^{-5} for Rg distributions and 4.7 x 10^{-4} for Rn distributions did not

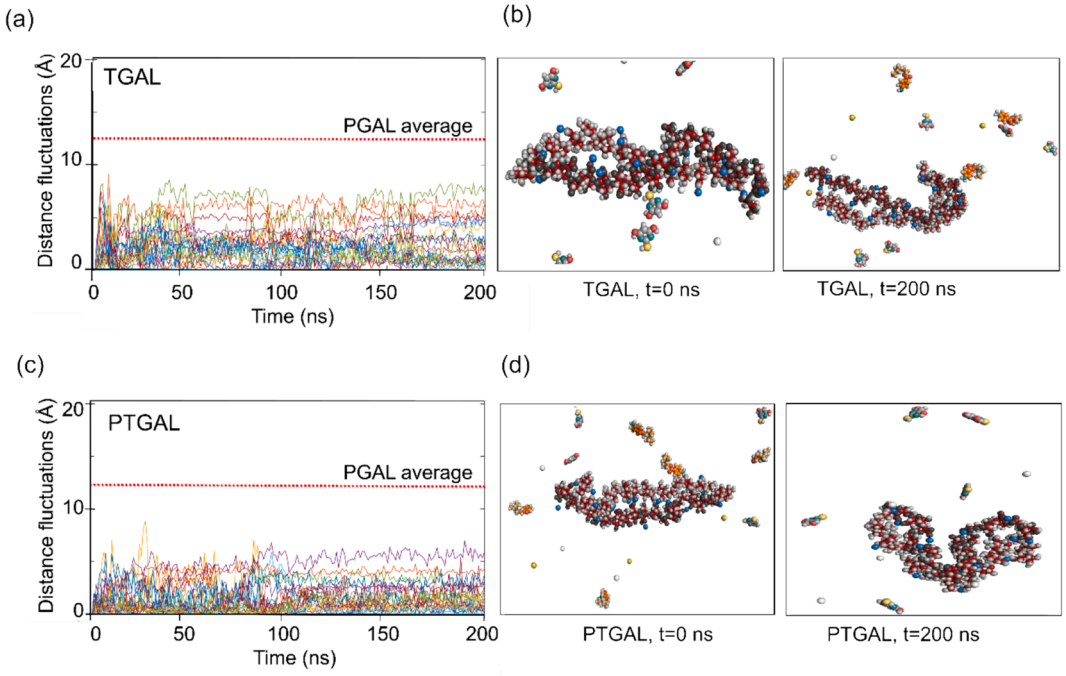

Fig. 2. Distance fluctuations between centers of masses of nearest GAL unit pairs, which face each other in the initial configurations of (a) TGAL and (c) PTGAL models. Dotted lines represent the average distance fluctuations of PGAL chains from ref. [53]. Snapshots of (b) TGAL and (d) PTGAL models.

support the hypothesis that the two distributions (TGAL and PTGAL) belonged to the same population.

For a more in-depth investigation of the dynamic non-bonded interactions (including dual cross-linking, electrostatic, and H-bonding) and stiffness of the models, the extent of the cross-linking and de-cross-linking between TGAL and PTGAL chains was monitored. The distances between the center of masses of the two nearest cross-linked galacturonic acid (GAL) units (abs(*di(t) − di(0)*) were plotted, where *di*(0) is the initial distance at $t = 0$ ns (Fig. 2a,c, Table S1). In a recent similar study, these distances were measured for PGAL chains in explicit water with an average distance of 12.75 Å [53]. The median and interquartile range (IQR) of |(d(t)-d(0))| distributions of PGAL were found to be 2.3 Å and 3.9 Å, respectively. Here, the initial cross-linking of TGAL and PTGAL chains seems to be more conserved as opposed to the PGAL system [53], as indicated by higher mean distance fluctuations of PGAL chains (12.75 Å) as shown in Fig. 2a,c with dotted lines. Furthermore, the addition of PC molecules to the TGAL system increased the stability of the cross-linkings between PGAL chains. The median and IQR values for TGAL were 2.1 Å and 2.8 Å, respectively, whereas these values decreased to 1.5 Å and 2.7 Å for the PTGAL system (Table S1).

Then, we visually controlled the position and motions of cross-linker Ca^{2+} ions (Fig. 2b, d). We observed that these ions lost their cross-linking position from time to time when interacting with a single COO^- group, but they were quickly regained. To understand the extent of intermolecular interactions between the components of the models (Ca^{2+} ions, PC, TBA, and GAL chains), the radial distribution function (RDF) was used (Fig. S3, S4). For all investigated systems, the peak at around 2 Å is quite apparent between COO^- groups and Ca^{2+} ions, indicating the Ca^{2+} induced gelation of chains with COO^- groups as reported in the literature (Fig. S3) [53–55]. On the other hand, other oxygen atoms on the chains (O2, O3, O4, and O5 positions that shown in Fig. S4) didn't display any significant interactions with Ca^{2+} (Fig. S4). Furthermore, in order to investigate the non-bonded interactions between the system components, RDF calculations were performed between the PC and TBA molecules as well as between the atoms of PC and TBA molecules and PGAL chains. According to the results, we observed an increasing amount of hydrogen bonds and electrostatic interactions in the PTGAL model compared to the TGAL model (Figs. S5, S6 and S7). The magnitude of van der Waals and electrostatic interactions was also found to be higher for the PTGAL model (Fig. S8). These findings suggest that the increased stabilization of PTGAL chains can be attributed to more stable non-bonded intra- and intermolecular interactions between TBA and PC molecules (Fig. S8).

As a result, MD simulations for TBA and/or PC-added PGAL systems indicated the stability of the cross-linking between polymeric chains, which would result in slow degradation and dual-cross-linking behavior of the pectin hydrogel. Furthermore, the addition of PC molecules to the PTGAL model seems to further promote nonbonded interactions, and enhance the stability of the hydrogel. This computational study at the micro level offers a comprehensive perspective on the pectin hydrogel, paving the way for a detailed understanding of its functional properties.

3. Experimental studies

This study introduces two distinct types of PC-loaded multifunctional hydrogel structures, namely PZ (zeolite added) and PTBA (TBA added) hydrogels, designed for use as wound dressings. These hydrogels were synthesized using a facile and cost-effective sol–gel method, with dynamic dual ionic bonds serving as the primary cross-linking mechanism. Synthesized PZ and PTBA hydrogel films were homogeneous without any cracks. They are transparent, which can enable to monitor of the wound. The results and discussion obtained from *in vitro* wound healing tests (Table S3) of the hydrogels are presented in Supporting Information in detail. In the following, morphological, thermal, rheological, self-healing, shape fitting, remoldability, release, *in vivo* wound healing and histological properties of the hydrogels are discussed.

3.1. Morphological analysis

Scanning electron microscopy (SEM) images of the dried cross-section films of PZ and PTBA samples are shown in Fig. 3 at three different magnifications. Both hydrogels have a smooth, irregular, spherical porous structure that facilitates solvent accommodation and procaine release. The PTBA formulation has more pores compared to the PZ formulation, which is expected to mimic the extracellular matrix (ECM) due to its high porosity [56]. Including TBA molecules in the PTBA hydrogel increases the diameter of spherical pores and creates some holes and cracks (Fig. 3). The PZ hydrogel film, containing zeolite particles (Fig. 3a, b) shows numerous sharp-edged crystals (marked with red arrows) that resemble the cubic zeolite-A morphology (Fig. 3a, b, c).

3.2. Contact angle analysis

The effect of zeolite particles and TBA molecules on the water contact angle of dry hydrogels was measured using sessile drop analysis. The water contact angle of the PZ hydrogel was found to be 47.7 ± 1.6°, while the water contact angle of the PTBA hydrogel was 57.1 ± 3.9° (Fig. 4). This is because zeolites' anionic nature and the pectin matrix's high charge can interact with water through hydrogen bonding, increasing the surface free energy and decreasing the contact angle. Conversely, the addition of TBA molecules to the pectin matrix reduces electronegativity, reducing the interaction with water molecules and increasing the contact angle [57]. This is due to secondary interactions of TBA molecules with procaine and pectin chains, as discussed in the computational section.

3.3. Thermal analysis

We analyzed the glass transition (T_g) and melting (T_m) temperatures and calculated the enthalpy (ΔH_m) of PZ and PTBA hydrogels through differential scanning calorimetry (DSC) analysis (Table 2). The Tg of the PZ and PTBA formulations are 46.2 °C and 46.8 °C, respectively, indicating that the pectin chains are not flexible at room temperature.

T_m of both formulations is similar. However, the ΔH_m of PZ hydrogel (81.8 ± 4.2 $J.g^{-1}$) is lower than that of PZ hydrogel (94.3 ± 2.3 $J.g^{-1}$). The inclusion of TBA molecules may have contributed to the improvement in structure stiffness and restricted the flexibility of pectin chains, leading to an increase in the number of crystalline regions in the pectin matrix [53,58,59]. The strength of molecular interactions within the crystalline domain is determined by factors such as the regularity of the chain structure (tacticity), chain stiffness, and the presence of interacting groups like H-bonds or electrostatic interactions. Since the PTBA hydrogel has more H-bond interaction sites and cross-linker capacity, the pectin chains require more thermal energy to melt. The enthalpy of melting (ΔH_m) is therefore influenced by the presence of both TBA and PC molecules. The results suggest that the incorporation of PC molecules into PTBA hydrogel led to substantial increase in H-bonding in pectin chains and backbone crystalline regions. These findings are consistent with MD simulations and swelling results, implying that the PTBA formulation has a lower swelling ratio.

3.4. Rheological analysis of the hydrogels

To gain a better understanding of the relationship between the microstructure of hydrogels and their rheological responses, which are directly related to their flexibility, a detailed rheological analysis was conducted. Test parameters of the rheological characterization are given in Table S4. We can categorize the measurements into three main areas for examination: (i) Stiffness, viscoelasticity, and shear-thinning properties were assessed through oscillation amplitude and frequency sweep analysis; (ii) Self-healing properties were evaluated via six-cycled thixotropic oscillatory strain amplitude sweep measurements [60]; and (iii) Stability, durability, and recovery abilities were tested by stress

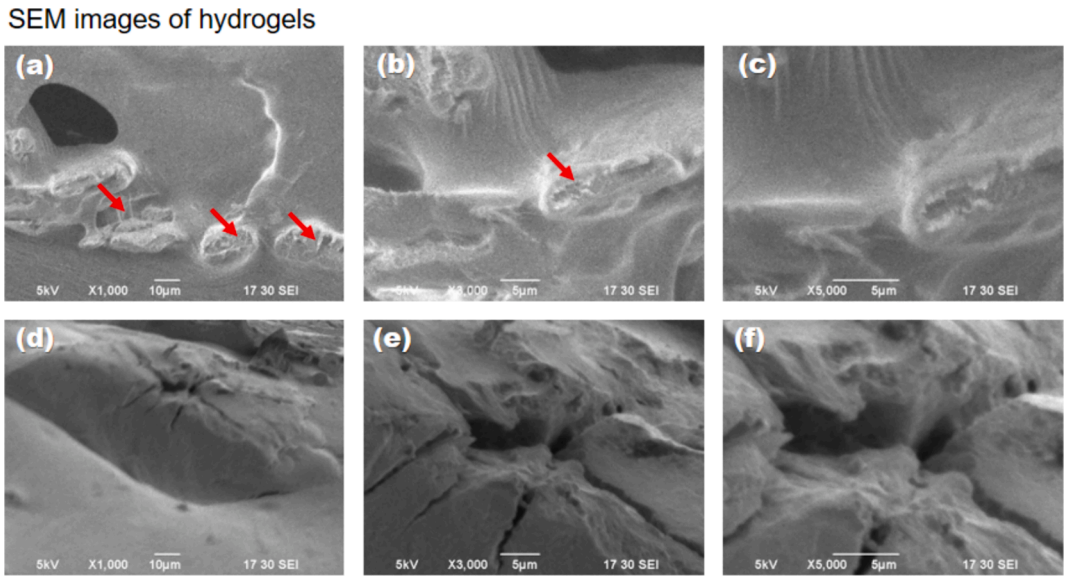

Fig. 3. SEM images of hydrogels. (a-c) Zeolite added PZ; (d-f) TBA added PTBA with different scales.

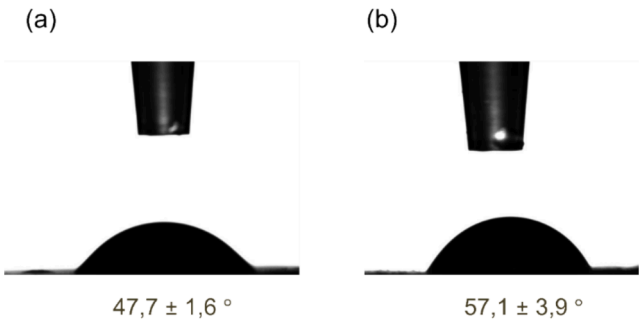

Fig. 4. Contact angle images of hydrogels. (a) Zeolite added PZ; (b) TBA added PTBA.

Table 2
DSC data for PZ and PTBA hydrogels.

	PZ	PTBA
Glass transition temperature (T_g, °C)	46.2 ± 0.3	46.8 ± 0.1
Melting temperature (T_m, °C)	221.8 ± 0.3	222.5 ± 0.6
Melting enthalpy (ΔH_m, $J.g^{-1}$)	81.8 ± 4.2	94.3 ± 2.3

relaxation and creep tests.

3.4.1. *Oscillatory strain and frequency sweep analysis*

The analysis of strain and frequency sweep offers a detailed understanding of the viscoelastic characteristics of materials, which is crucial for comprehending their response to various deformation scenarios. Strain sweep analysis reveals that in both hydrogel types, the linear viscoelastic region predominantly exhibits solid-like characteristics. This is evidenced by the storage modulus (G', indicating the material's capacity to store energy under deformation) being consistently higher than the loss modulus (G'', reflecting the material's energy dissipation ability) as seen in Fig. S9 [61]. The storage modulus of both formulations is highest at the smallest strain amplitude (γ0; G'0) and decreases to a lower value at the highest strain amplitude (γ∞; G'∞) (Fig. S9a, Table S5). This trend is likely due to the disruption or rearrangement of the numerous hydrogen bonds and electrostatic interactions during deformation at the flow point [59]. Furthermore, the integration of zeolite particles within the PZ matrix enhances resistance to deformation, a result of robust polymer-zeolite and zeolite-zeolite interactions [62]

For both hydrogels, the strain amplitude at the flow point (γ_f) is the same, where the internal structural failure results in viscous behavior (crossover (gel) point, Gf; G'=G") (Table S4). On the other hand, PTBA hydrogel has a greater storage modulus at the flow point G'_f (Table S5). The connected network of filles, i.e., zeolite particles, disrupts as the strain amplitude increases, which causes the formation of massive agglomeration chains and cluster breakup in the PZ hydrogel [63]. The increase of the aggregates and polydispersity in the polymer network indicates an increase in the loss modulus, as seen in the increasing amount of G'' in PZ with strain amplitude [64].

Both G' and G'' as a function of angular frequency are shown in Fig. S9b. The data revealed that both G' and G'' values show a slight dependence on frequency in the range tested, with G' consistently being greater than G''. These results suggest that PTBA and PZ hydrogel films have solid-like viscoelastic structures with extensive interconnectivity [17]. The correlation between frequency and dynamic modulus adheres to the Power Law model (Eq. S1), k' (gel strength) and n' (indicator of the gel strength) coefficients for both hydrogels are listed in Table S5 and elaborately discussed in the Supplementary Information. Calculations suggest that PTBA hydrogel is a more robust gel [65].

The hydrogels' shear thinning properties were investigated by a frequency sweep test under oscillatory mode using complex viscosity curves (Fig. 5a). The results demonstrate a linear decrease in complex viscosity corresponding to the frequency on a double logarithmic scale, marked by a significantly steep slope (0.9), indicative of a pronounced shear-thinning behavior in the formulations [66]. This phenomenon facilitates the alignment of polymer chains with the flow direction, enhancing the shape-fitting (Fig. 5b), remolding (Fig. 5c), and self-healing (Fig. 5d, e) capabilities of the structures. As shown in Fig. 5b, the PZ and PTBA hydrogels exhibit dynamic adaptability to finger movements, owing to their shear thinning and self-healing properties [67,68]. This feature enables them to endure diverse body movements and deformations at various angles, rendering them ideal for advanced wound dressing applications. To further illustrate their shape adaptability, dried hydrogel films were placed in a semi-spherical mold (Fig. 5c) and subsequently swollen in a pH 8.0 buffer solution mimicking wound exudate. As observed in Fig. 5c, the hydrogels swiftly conformed to the mold's shape without any cracking and maintained this shape even upon drying, underscoring the self-healing and shear-thinning properties of these synthesized pectin-based hydrogels [69,70].

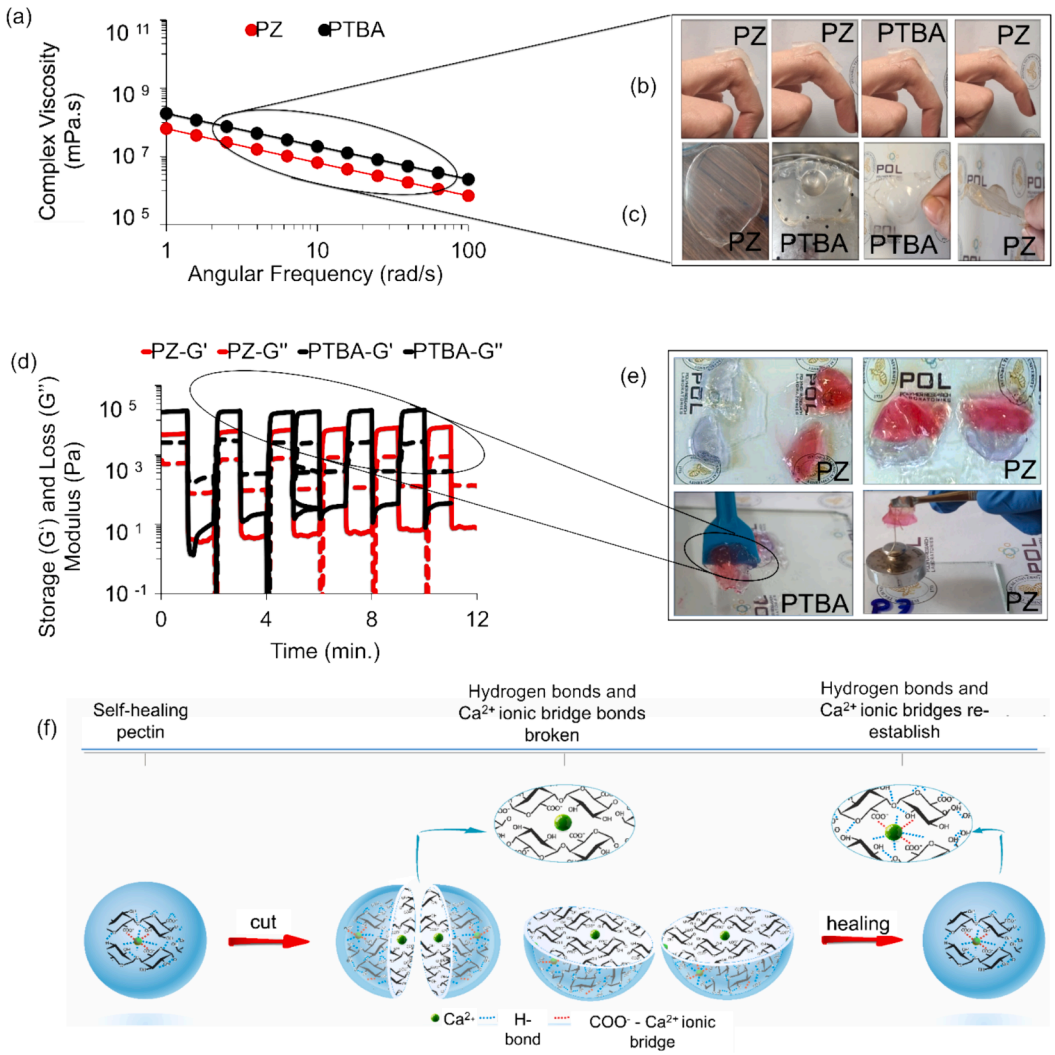

Fig. 5. (a) Complex viscosity of PZ and PTBA hydrogels by oscillation frequency sweep, (b) The tensile of hydrogels on the surface of different postural fingers, (c) Photographs of shape filling and remolding process: Dry hydrogel swelled in pH 8.0 media and placed in a semi spherical-shaped container. It dried without any crack and remolded the container' s shape, (d) Rapid self-healing determination of PZ and PTBA hydrogels by oscillation strain steps (1% strain to 1000% strain and back to 1% strain, each step for 1 min), (e) Photographs of the self-healing process of the hydrogels: Two pieces of PZ and PTBA stained with different colors; hydrogel cylinders were brought into contact with each other in line for a visualized self-healing test with no external force applied. The hydrogel cylinders were self-healed within 10 min. The self-healed PZ and PTBA hydrogels lift and support themselves and dried hydrogels withstoodd a weight of 50 g, (f) Schematic illustration of self-healing mechanism and dual dynamic secondary interactions on galacturonic acid monomer. (*We only used one because both materials produced the same photograph for (b), (c), and (e)).

3.4.2. Thixotropic strain sweep measurements

Thixotropic strain sweep analysis, a critical technique, was utilized to evaluate the self-healing or recovery characteristics of hydrogels following the application of constant shear. This aspect is pivotal in determining the hydrogel's capacity to flow into and mend cracks or voids, a fundamental aspect of self-healing. Thixotropy refers to a material's propensity to flow under shear due to a reduction in viscosity and subsequently recover its original state upon the removal of high shear force [15,71,72]. Hydrogels with efficient self-healing capabilities could enable rapid recovery when the surface of the hydrogel is damaged by frequent body movements [73]. Thereby, these materials improve the lifespan of the wound dressing [22]. Pectin hydrogel inherently exhibiting shear thinning and self-healing properties since it has a considerable amount of dual dynamic and reversible physical interactions, as demonstrated by MD studies [13–15].

The self-healing properties of the PZ and PTBA hydrogels are investigated through rheological evaluations and macroscopic tests involving visual inspections. The rapid recovery ability of the materials after network breakdown at high strains was demonstrated by performing a six-cycle thixotropic measurement (Fig. 5d). The test started at a low strain (1%) step for 1 min, followed by a high strain (1000%) step for 1 min per cycle. The thixotropy diagram displayed a solid-like behavior at low strain with $G' > G''$ and a liquid-like structure at high strain with G'' > G'. Both hydrogel formulations exhibited full recovery, with a rapid sol-to-gel transition and no decrease in G' observed throughout the cycles. The PZ hydrogel demonstrated 97.2% recovery after six cycles, while the PTBA hydrogel exhibited a remarkable 100% recovery, as shown in Table S5 and Fig. 5d. These results demonstrate the outstanding self-healing capabilities of both hydrogel formulations [73]. The exceptional self-healing feature is attributed to the high level of dynamic charges in the pectin matrix, which combines strong hydration, reversible H-bonding, and metal coordination between Ca^{2+} and COO^{-} as identified by RDF results of MD simulations (Fig. 2). The reversibility of ionic associations rapidly triggers the healing process. Additionally, it's noteworthy that the hydrogel's healing efficiency is substantially influenced by the extent of its cross-linking, as indicated in studies [74,75,76]. Literature reveals the development of hydrogel films using pectin with self-healing properties.

Literature highlights the development of hydrogel films using pectin hydrogel with self-healing properties. However, in contrast to our facile and biocompatible preparation method, these hydrogels often require chemical modifications, which might negatively affect the cyto-compatibility and other functionalities of the hydrogel.

Macroscopic visual analysis further examined the self-healing phenomena (Fig. 5e). The results of the visual self-healing test showed that the cut hydrogel was completely healed in 10 min, and the contact surface of the hydrogels was fused, as observed by the formation of a diffusion layer. The healed hydrogels could support a weight of 50 g even after drying, demonstrating their strong self-healing properties. Compared with the difficulty in the "movement" of molecules at a higher degree of cross-linking, a low degree of cross-linking degree results inadequate self-healing due to lower ionic bonds and excess vacancies (or free volume) within the matrix for healing recovery. At an optimum degree of cross-linking, the free volume allows the molecules to 'move' easily, resulting in an increase in healing efficiency [75]. The cross-linking concentration used for both PZ, and PTBA hydrogels is an optimum value for self-healing properties. A schematic illustration of the self-healing mechanism and dual dynamic secondary interactions on the galacturonic acid monomer is shown in Fig. 5f.

3.4.3. Creep-recovery and stress relaxation

Creep recovery and stress relaxation analyses are utilized to comprehend the viscoelastic behavior of materials. These measurements are crucial for assessing the durability and reliability of materials in long-term applications [77,78].

Creep recovery analyses were conducted at 25 Pa for a 300 s creep phase followed by a 600 s recovery phase. According to the creep-recovery results, both PTBA and PZ hydrogels exhibit a combination of elastic solid–viscoelastic and elastic viscous fluid properties. The results are in accordance with the literature as expected for gels with flexibility [79]. PTBA hydrogel had a higher compliance value; thus, it can be strained more efficiently (Fig. 6) [80]. However, PTBA hydrogel showed a higher RC% (55.61) when compared to PZ (40.34) (Equation S2, Table S5). PZ hydrogel has low *Jmax, Jmin,* and RC% values; here, the zeolite particles inside the matrix act as a barrier to the strain and probably result in phase separation when the shear is applied. On the contrary, enhanced interlayer interactions through cooperative hydrogen bonds and electrostatic interactions in PTBA hydrogel result in a viscoelastic material with a higher RC% value. Creep-recovery results demonstrate that TBA addition to the hydrogel (PTBA) allowed the formation of more elastic gels, which may be related to TBA and PC interactions.

The stress relaxation modulus of hydrogels at four different temperatures (15, 25, 35, and 45 °C) was monitored to understand the temperature dependence of the characteristic relaxation time (τ) (Fig. 6b,c, Fig. S10a, b and Tables S6, S7). The resulting stress relaxation curves were normalized as the ratio of stress to initial strain (G/G0), plotted on a logarithmic scale, and the characteristic time (τ) was defined as the time required to reach 37 % of the initial stress [81]. Because of the reversibility of cross-linking ionic bondings and H-bonds and superior self-healing ability of the PZ and PTBA formulations, both samples are expected to rearrange the gel structure through dynamic electrostatic interactions and hydrogen bondings. Distinctly, both hydrogels released stress faster at higher temperatures. With the exception of PTBA at 15 °C, both samples significantly released stress at the temperatures being measured. Here, the association of H-bond interactions at lower temperatures is strong and can act like a weak cross-link between the chains [44]. On the other hand, due to dissociation of H-bond interactions at higher temperatures, the samples released stress more efficiently. Moreover, the hydrogels are characterized with activation energy (Ea) (Equation S3, S4, Fig. S10, Tables S6, S7). The Ea value of PTBA (82.38 kJ/mol) is significantly higher than the Ea of (37.68 kJ/mol) PZ hydrogel, indicating the dynamic exchange of the secondary bonds inside the hydrogel matrix. High stability, which is related to a high amount of secondary bonds, restricts chain mobility, hindering bond re-shuffling and raising activation energy [82].

3.5. Swelling

Hydrogel dressings have a high capacity to effectively absorb wound exudate and create a moist environment that promotes wound healing. However, this swelling process can also cause structural changes in the hydrogel matrix, impacting the mobility of drugs and cross-linkers and therefore affecting drug release. Water, acting as a plasticizer, reduces the glass transition temperature (Tg) of the system, facilitating the polymer chains' transition from a glassy to a rubbery state [83]. Due to the inclusion of water, pectin hydrogel swells, resulting in dramatic changes in polymer and drug concentrations, and increasing the dimensions of the system.

Polymeric hydrogels swelling is governed by two fundamental mechanisms: diffusion-controlled (Fickian) and relaxation-controlled (non-Fickian). The swelling mechanism depends on the diffusion of water molecules into the hydrogel's porous framework, subsequently initiating the relaxation of the macromolecular chains [35]. Particularly in pectin-based hydrogels, the abundance of ionizable COOH groups is a critical factor. These groups cause the pectin's inherently coiled chains to expand, markedly increasing the swelling capacity of the hydrogel [36]. Additionally, the presence of $–COO^-$ groups within the pectin structure causes intermolecular repulsion, further facilitating the relaxation of these chains.

The swelling ratio of hydrogels increased until it reached a maximum, after which degradation began. Understanding the degradation behavior of hydrogels is crucial in their evaluation as wound dressings. Fig. 7a illustrates the swelling profiles of PZ, PTBA, and pectin hydrogels (P) in pH 6.4 TRIS buffer. The swelling of P (9.89 ratio/h) and PZ (3.2 ratio/h) hydrogels was more rapid compared to PTBA (2.79

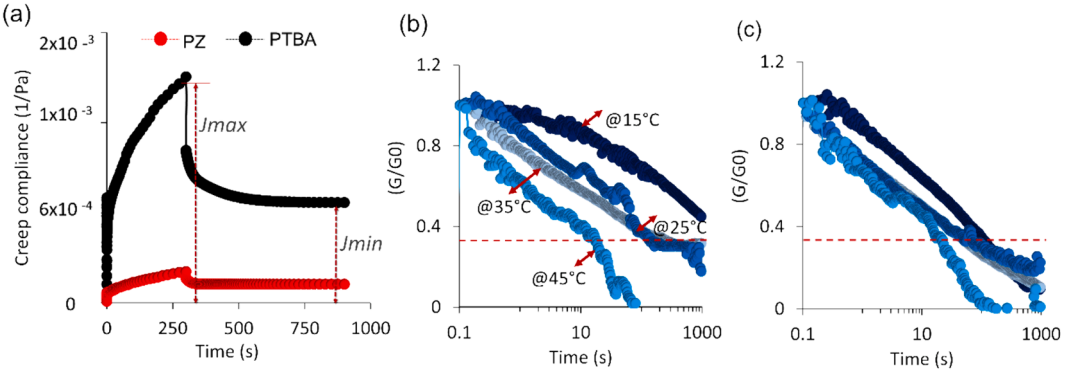

Fig. 6. (a) Creep analysis, and stress relaxation analysis of (b) PTBA, (c) PZ hydrogels.

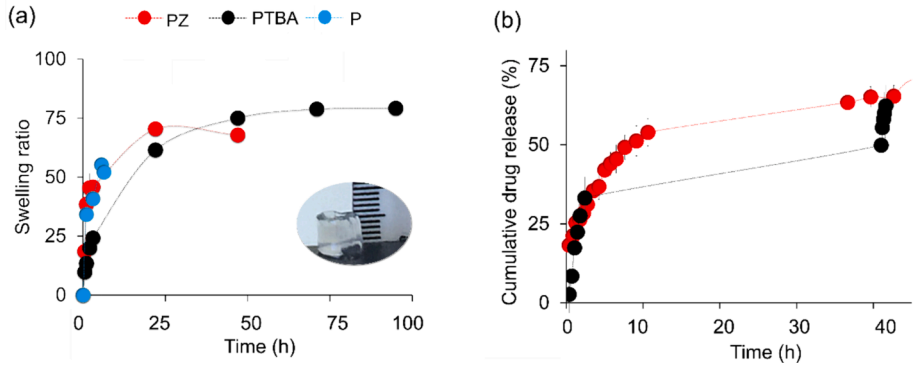

Fig. 7. (a) Swelling behavior P, PZ and PTBA hydrogels, (b) Drug release profile of PZ and PTBA hydrogels.

ratio/h). Notably, The P hydrogel demonstrated an accelerated swelling rate relative to PTBA and PZ hydrogels, which exhibited a more gradual degradation process. This reduced rate of swelling in PZ hydrogels can be attributed to the high crystallinity of Zeolite A, which serves as a robust physical cross-linking juncture within the hydrogel structure, thereby enhancing the overall stability of the hydrogel matrix [17,36]. These results are consistent with the SEM analysis and MD simulations, which suggest that PC and TBA molecules contribute to an increased formation of secondary bonds within the polymer matrix, as illustrated in Figs S5, S6, and S7.

3.6. Drug release profile

The release profiles of procaine (PC) from PZ and PTBA hydrogels are illustrated in Fig. 7b. The initial concentration of PC for the PZ hydrogel was selected as 30 mg/g-hydrogel, and the loading medium was maintained at a pH of 9.1. This choice was informed by comparative analyses of release profiles obtained at two distinct procaine concentrations (30 and 60 mg/g hydrogel) and across a range of pH levels (6.4, 9.1, 9.8), as shown in Fig. S11. Additional details can be found in the Supplementary Data. The PTBA hydrogels were synthesized as an extension of our previous research [84].

Initially, during the UV scan analysis, our aim was to detect any peaks corresponding to the pectin hydrogel. Importantly, the hydrogel composed exclusively of pectin (identified as P) did not show a notable release peak. Therefore, the contribution of the pectin (neat) hydrogel was considered insignificant and consequently excluded from the cumulative PC release calculations (Fig. S12).

There exists a significant correlation between the swelling ratio and the drug release pattern of the hydrogels (Fig. 7a, b). In a swelling-controlled system like these, the release of drugs is influenced not only by their diffusion from the polymer matrix but also by the diffusion and dissolution (chain relaxation) of the polymer chains within the matrix. This phenomenon, often termed “anomalous transport,” is characteristic of swelling-controlled systems, combining both diffusion and chain relaxation dynamics [85]. Our kinetic calculations provide empirical evidence supporting this phenomenon (Fig. S13, S14). Rassu et al. (2016) highlight that in particle-containing polymeric systems, drug release is typically governed by two primary mechanisms: drug diffusion and polymer degradation [86]. Our experimental results corroborate this, showing that both hydrogels exhibit a burst release phase, releasing approximately 60% of initial PC in a controlled manner within approximately two days, indicative of long-term controlled release (Fig. 7b). This initial burst release is particularly advantageous for wound healing applications, providing immediate relief followed by a controlled, prolonged release for gradual healing [87]. Zare et al. demonstrated that the initial burst release phase is largely due to drug diffusion or the presence of drugs near the surface that rapidly diffuse into the buffer solution. Subsequently, as the polymer matrix begins to degrade, the simultaneous drug diffusion and matrix degradation can accelerate the drug release rate [86]. The hydrophilic nature of procaine molecules further contributes to the initial burst release phase [85].

The PTBA hydrogel, characterized by a stiffer and more compact structure with slower degradation due to robust molecular interactions (as detailed in the Molecular Dynamics (MD) section), exhibits a prolonged relaxation time and consequently a reduced initial burst release compared to the PZ hydrogel. Berg et al. [88] supports this, showing that drug release from polyelectrolyte multilayers is dependent on the structural characteristics of the film, such as pore size and the number of bilayers. Secondary interactions among the components in our study also alter the drug release pattern by modifying the morphology of the structures.

Regarding zeolite-A or TBA incorporation into hydrogels, our previous studies have shown significant alterations in drug release patterns. Our earlier research revealed that the addition of TBA significantly extended the release duration of theophylline from 4 hours to as much as four days, as noted in our previous publication [84]. This finding aligns with Pakulska et al. (2016), who demonstrated that increasing PLGA nanoparticle concentration in hydrogels correspondingly prolongs the drug release rate. Similarly, Shi et al. (2016) reported that nanoparticle integration within hydrogels facilitates a more gradual drug release [89,90].

With zeolites, as with any microporous system, the rate of drug release is controlled by the process of diffusion from the microporous channels [91]. In our previous study, we observed that the PC molecule exhibited a release duration of 8 hours, followed by a plateau phase. Contrasting this, our current study demonstrates that, when the PC molecule is encapsulated within zeolite-A particles surrounded by a pectin matrix, the PC molecule is released in a controlled manner over an extended period of approximately 40 hours [92]. The same controlled release pattern was also evident in our previous studies involving zeolite-A and theophylline [36,93].

Despite PC’s inherent water solubility, its sustained and controlled release from the pectin-zeolite (PZ) and pectin-2-thiobarbituric acid (PTBA) hydrogel matrices can be primarily attributed to the robust intra- and intermolecular hydrogen bonding of the PC molecules. This characteristic is analyzed in detail in the Molecular Dynamics (MD) section of our study. Two amino groups are present in the procaine molecule, a primary amine and a tertiary amine. Therefore, depending on the acidity of the medium, PC can exist as a neutral molecule (No), a monocation (NoH^+), or a dication (NoH_2^{+}). Hydrogen bonding plays a pivotal role in moderating the release dynamics of PC, effectively slowing its diffusion through the hydrogel matrices. Moreover, due to the extensive intra- and intermolecular hydrogen bonding of PC molecules, clusters of these molecules might be formed within the matrix. These clusters act as barriers along the diffusion pathway. This phenomenon also provides a plausible explanation for the incomplete final release of PC, as these clusters remain entrapped within the matrix. The

degradation of the diffusion path further complicates the release process, resulting in the entrapment of larger procaine clusters within the matrix. As a result, PC exhibits a sustained release profile, which is not typically expected from a water-soluble molecule. This phenomenon underlines the complex interplay between the physicochemical properties of the drug and the structural attributes of the hydrogel matrices, leading to a controlled release mechanism that defies the conventional expectations of solubility-driven diffusion. Toews and Bates (2023) reported in the same line with us. They reported that as hydrogen bonding is the best mechanism allowing for the controlled, sustained release of drugs from a hydrogel matrix, the backbone selection was catered to ensure it was achievable with hydrophilic drugs [94].

3.7. Drug release kinetic

The drug release data from our study were analyzed using various kinetic models, with the findings presented in Table 3. The models which include zero order, first order, Kornsmeyer-Peppas, Higuchi and Hixon-Crowell, are fundamental in understanding the mechanisms controlling drug release from various formulations (Table 4 and Table S8). This methodology provides a systematic approach to analyze drug release data and identify the governing release kinetics, which is crucial for the development and optimization of effective drug delivery systems.

The effectiveness of these models in characterizing the drug release kinetics is quantified by the regression coefficient value (R^2), where a value closer to 1 indicates a more accurate fit.

In our observation of the 40-hour release period, both PZ and PTBA hydrogels demonstrated the most significant adherence to the Korsmeyer-Peppas model, as indicated by the highest R^2 value of 0.9774 and 0.990, respectively (Table 4, Table S8, Table 3, Figs. S13, S14). This semi-empirical equation is viewed to be the most comprehensive mathematical model used to determine the drug release proile of water-swellable polymers. The applicability of this model is limited to the first 60% of the released solute (Mt/MN < 0.60), when the drug release is proportional to time [95]. According to this kinetic release model, for PTBA, n = 0.7 indicates a non-Fickian (anomalous) release mechanism, where both diffusion and relaxation influences are significant [96,97]. With increasing water content, the diffusion coefficient of the drug increases substantially [83]. Initially, diffusion dominates the drug release, primarily through the hydrogel's surface layers. As time progresses, the role of diffusion diminishes while pectin chains relaxation becomes increasingly significant for releasing drug molecules that are located deeper in the matrix. This n value, ranging between 0.45 and 0.89, represents the non-Fickian diffusion, indicating a release predominantly governed by swelling-controlled diffusion, accompanied by minor surface erosion. This finding aligns with existing literature on pectin hydrogel kinetic studies [95,98–100]. For instance, Grolut et al. described their pectin based hydrogel using the Korsmeyer-Peppas model with an n = 0.58, typical for anomalous transport, where both solvent diffusion and polymer relaxation are key considerations [100].

In comparison, the inclusion of zeolite-A particles in the pectin matrix (PZ) reduced the n-value to 0.35, indicative of Fickian diffusion, suggesting a slower drug diffusion rate relative to the relaxation rate. This phenomenon can be attributed to the zeolite particles acting as obstacles to diffusion, thereby hindering the motion of pectin chains and ultimately affecting macromolecular motion. Pore tortuosity, influenced by the distribution of nanoparticles during nanocomposite preparation, also plays a role in this anomalous release mechanism. A similar explanation is reported by Silva et al. They found that the release mechanism of Vit-B12 from hydroxyethyl methacrylate-added pectin hydrogels was predominantly anomalous. This suggests that the release is governed by a combination of Fickian diffusion and macromolecular relaxation. The same release mechanism was observed for the pectin-TiO_2 nanocomposites, but with a tendency towards Fickian diffusion (n < 0.45) [95]. The disruption of these bonds leads to a gradual process of chain relaxation. During the initial 60% of the release, primarily in tris buffer, erosion is not significant.

Rheological results, particularly those focusing on strain sweep analysis, revealed a gradual decrease in the storage modulus (G') and a slow increase in the loss modulus (G″) (Table S5, Fig. S9). This behavior indicates chain relaxation within the PTBA matrix, which can be attributed to the breaking of inter- and intramolecular secondary bonds within the PTBA components. In creep-recovery analysis, the PZ hydrogel exhibited a lower strain and creep compliance compared to PTBA, most likely a result of the zeolite particles' restrictive effect on the mobility of pectin chains, acting as a barrier to strain, potentially leading to phase separation under applied shear stress as elucidated by the release kinetics.

Other kinetic models, including first-order, Hixson-Crowell, and zero-order, displayed lower fitting quality, as evidenced by their lower regression coefficients. Nonetheless, these models offer valuable insights and contribute to a more comprehensive understanding of the drug release characteristics inherent to the system.

Table 4
Kinetic model equations [156–159].

Model	Equation	Parameters and descriptions	Graphical presentation
Zero −Order	$Q_t = Q_0 + Kot$	Q_t: concentrationount of drug released at time t, Q_0: initial drug concentration in solution, *Ko*: zero-order release constant.	Cumulative percentage of drug release versus Time
First-order	$Log_C = log_{C0} - K1_t/2.303$	*C*: percentage of drug remaining at time t, *C*0: initial drug concentration, K_1: First-order release constant expressed in time^(−1).	Logarithmic percentage of drug remaining versus Time
Higuchi	$Q = K_H t^{1/2}$	*Q*: Cumulative amount of drug released in time t, K_H: Higuchi dissolution constant	Cumulative percentage drug release versus Square root of Time
Korsmeyer-Peppas	$\frac{M_t}{M_\infty} = K_P t^n$	*Mt/M∞:* racFtion of drug released at time t, K_P: Korsmeyer release constant, *n*: diffusion exponent.	Logarithmic cumulative percentage drug release versus Log Time
Hixon-Crowell	$W_0^{1/3} - W_t^{1/3} = K_H t$	W_0: the initial amount of drug, W_t: the remaining amount of drug, K_H: Hixson release constant	Cube root of drug percentage remaining in matrix versus Time

Table 3
The regression coefficient of kinetic models fitted for PZ and PTBA.

Code	Zero-order		First-order		Higuchi		K.-Peppas		Hixon-Crowel	
	K_0(μg.mL^{-1}.t^{-1})	R^2	K_1(t^{-1})	R^2	K_H(μg.mL^{-1}.t$^{-1/2}$)	R^2	K_{1P}(t^{-n})	R^2	K_{S0}(μg$^{1/3}$.mL$^{-1/3}$)	R^2
PZ	0.0178	0.82111	0.0001	0.6837	1.2665	0.9249	0.35	0.9774	−0.0008	0.8323
PTBA	0.0389	0.835	0.0004	0.42421	1.75	0.835	0.7	0.9909	−0.0015	0.7705

3.8. In vitro blood clothing property

The assessment of the coagulation effectiveness of P, PZ, and PTBA samples was conducted through the analysis of the Blood Clotting Index (BCI) as outlined in Equation (6). It is pivotal to note that a reduced BCI value indicates a higher proficiency in blood clotting. The BCI values for PZ (25.02 ± 9.2) and PTBA (25.89 ± 9.5) samples were found to be significantly lower neverthless, the blood build-up effect of PC molecule, nearly half, compared to P (56.65 ± 15.7) (Fig. 8a, b). Although PC is a local anesthetic which does not include dopamine structure, it does not directly contribute to blood clotting. Instead, it may increase blood accumulation, thereby aiding in dilation. This observation emphasizes their superior coagulation capabilities of the hydrogels, as shown in Fig. 8a, b. The structural composition of these hydrogels, characterized by their intricate, interconnected porous architecture and substantial swelling properties, enables them to absorb substantial quantities of blood. This absorption facilitates the concentration of red blood cells and platelets, thereby enhancing the hemostatic process [101]. Additionally, according to Quan et. al. the presence of COO^- groups in pectin chains may further enhance the hemostatic process by stimulating the interface of red blood cells and platelets [102]. Furthermore, the inclusion of zeolites in the PZ hydrogels plays a ciritical role in their hemostatic efficacy. Zeolites are microporous aluminosilicate minerals are distinguished for their ability to adsorb toxins from the blood, thereby promoting coagulation [5,6]. In the case of PTBA, the presence of cationic moieties and thiol groups is hypothesized to activate tissue factor (TF) and platelets, consequently accelerating blood coagulation [103]. Moreover pectin-calcium hydrogels owe their hemostatic characteristics to calcium ions and the ability of the alginate hydrogel to serve as a matrix for the accumulation of erythrocytes and platelet accumulation. In addition, release of Ca^{2+} ions from the wound dressing to the wound site might enhance the generation of pro-inflammatory cytokines, such as interleukin (IL)-6), IL-1, tumor necrosis factor (TNF), and the chemotactic cytokine IL-8. A similar observation was reported by Pereira et al. [104].

This phenomenon is further enhanced by the inherent characteristics of pectin hydrogels – their soft, hydrophilic nature, high water absorption and retention capacities, and an their ability to adsorb plasma proteins, which are vital for blood coagulation [17,105]. Additionally, the stiff network and increased swelling ratio of PTBA contribute significantly to its clotting efficacy. The structural integrity of PTBA hydrogels potentially plays a crucial role in facilitating this hemostatic action.

3.9. Antioxidant property

When the skin is damaged, large amounts of ROS are produced in the inflammatory phase of wound healing, which cause biological damage such as the breakdown of lipids, proteins, and nucleic acids, and ultimately cell death, leading to delayed healing or even tissue destruction. Antioxidants can help to prevent oxidative damage and promote a healthy wound healing environment by scavenging free radicals and preventing oxidative stress [106].

According to the results illustrated in Fig. 8c, both formulations have a certain degree of free radical scavenging capacity. This is due to the antioxidant capabilities of the pectin polymer, which have been

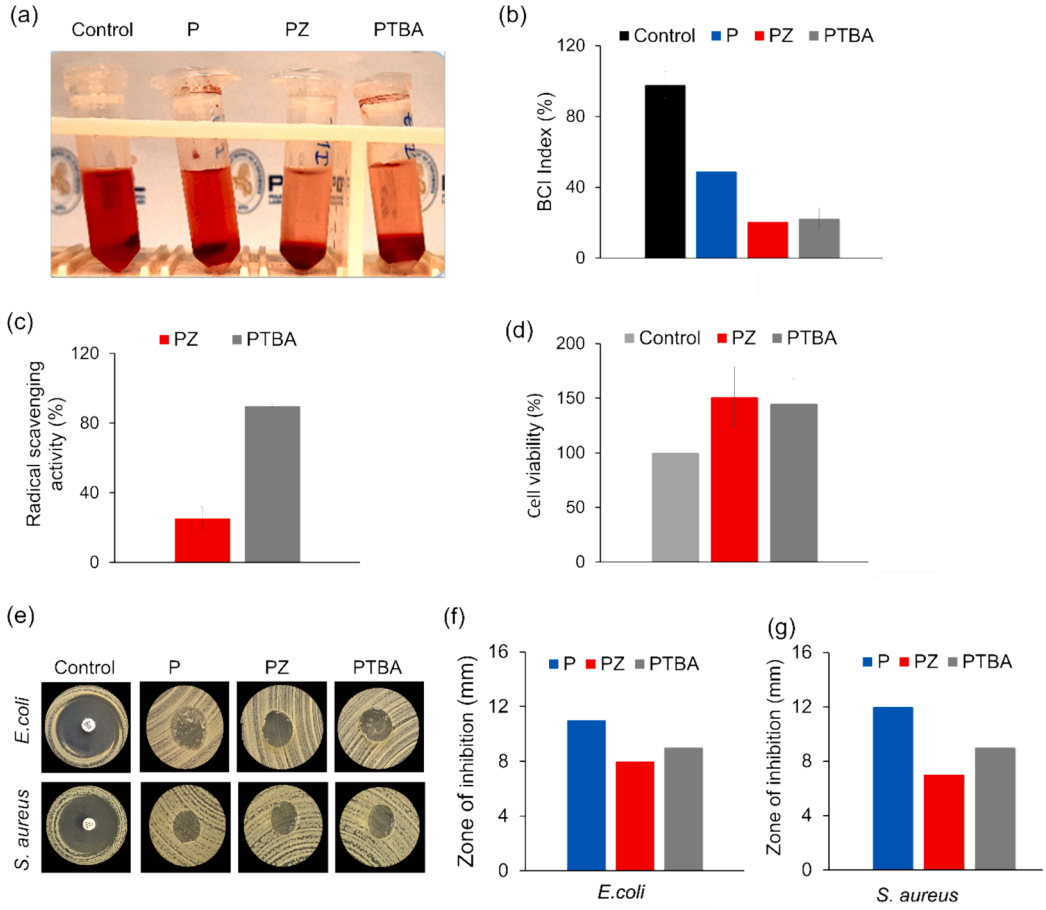

Fig. 8. (a) Visual images of hemostatic assay, (b) Blood clothing index, (c) Antioxidant evaluation, (d) Cell viability, (e) Visual images of antibacterial zone of hydrogels to *E. coli* and *S. aureus* after incubation for 24 h, (f) Quantified antibacterial zone of hydrogels to *E. coli,* (g) Quantified antibacterial zone of hydrogels to *S. aureus.*

demonstrated through several phenomena, including (i) scavenging of free radicals such as hydroxyl and superoxide radicals, reducing their oxidative potential and preventing oxidative damage to lipids, proteins, and DNA; (ii) chelation of metal ions, such as iron and copper, which can contribute to the generation of reactive oxygen species (ROS) and oxidative stress. In this way, pectin helps to prevent the generation of ROS and protect against oxidative damage; (iii) anti-inflammatory effects, which can help to reduce oxidative stress and inflammation and support the healing of wounds and tissues subjected to oxidative stress [107]. Besides all these, crosslinker Ca^{2+} ions play a role in regulating oxidative stress and antioxidant defense. Some studies have indicated that calcium may influence antioxidant defense by modulating the activity of antioxidant enzymes and reducing oxidative stress [108–110].

It is worth mentioning that the free radical scavenging efficiency of PTBA hydrogel is 89.84 ± 2.08% (Fig. 8c). This efficiency surpasses that of other hydrogels prepared with pectin [10,111]. This exceptional performance can be attributed to the presence of sulfur ions within the 2-thiobarbituric acid, which participate in numerous essential metabolic processes [112,113]. Small molecules containing sulfur and selenium compounds are also studied for their antioxidant properties and ability to prevent disease [113]. The protective effects of sulfur and selenium compounds against disease can be attributed to radical scavenging and enzymatic decomposition of oxygen metabolites [114]. Sulfur is a critical component of the antioxidant molecule glutathione, which acts as a ROS scavenger and helps to maintain cellular redox balance [115]. Metal binding may enhance GPx activity and ROS scavenging for sulfur ions [113].

3.10. In vitro cytotoxicity

The results, presented in Fig. 8d, demonstrate that the PZ and PTBA formulations improve cell viability when compared to the control group. These results suggest that these formulations will encourage cell growth and survival in the wound area, reducing inflammation, preventing infection, and facilitating more effective cell repair and regeneration. The inherent biocompatibility of the pectin polymer is well-established in the literature, as indicated by numerous significant studies focusing on wound dressings made from pectin that exhibit high cell proliferation ratios [76,116–118].

However, despite these advancements, there remains a gap in the literature regarding the use of hydrogels for controlled delivery that specifically improves cell viability. This highlights the innovative aspect of our PZ and PTBA formulations in bridging this gap and offering a promising avenue for enhanced wound healing applications.

3.11. In vitro antibacterial analysis

Effective wound care requires preventing bacterial infections, which can lead to slow or delayed healing, scarring, and other complications [119]. Song et al. prepared pectin-chitosan hydrogel with ciprofloxacin release, and Hasan at. al prepared alginate/pectin/hyaluronic acid hydrogel with clindamycin release which effectively exert antibacterial activity [118,120]. However, in order to avoid antibiotic-resistant bacteria, advanced wound dressings must possess intrinsic antimicrobial activity.

To assess the antibacterial efficacy of P, PZ, and PTBA formulations against *E.coli* and *S.aureus*, an inhibition zone assay was conducted. The results indicate that the P, PZ, and PTBA hydrogels exhibited inhibitory effects with diameters of 11 mm, 8 mm, and 9 mm against *E.coli* and 12 mm, 7 mm, and 9 mm against *S.aureus*, respectively (Fig. 8e, f, g). These findings suggest that the synthesized hydrogels retain their antibacterial properties while enhancing cell viability (Fig. 8d) without the inclusion any antibiotics.

3.12. In vivo compatibility of hydrogel wound dressings

In *in vivo* studies, the commercial Kaltostat® wound dressing, known to be effective for wound healing but costly, was also used as a positive control group next to the control group. Kaltostat® is a wound dressing produced by ConvaTec Limited and has been clinically used for over 25 years for various types of wounds. It has been proven to be clinically safe and effective. In a study conducted by Brenner and colleagues in 2015, they demonstrated that it is an optimal wound dressing, especially for healing children's wounds, when compared with hydrofiber wound dressings [121]. It is demonstrated in the literature that it can be used for different indications. Its effectiveness has been determined in pressure sores [122], diabetic foot wounds [122], and acute carotid endarterectomy wounds [123]. Kaltostat® is an alginate-based wound dressing. Alginate is an anionic polysaccharide that has a mirror image structure similar to pectin. Due to its significant structural similarity to pectin hydrogel and its substantial successful use in clinical studies, it has been chosen as the positive control group. In animal experiments, the negative control group consisted of rats that did not receive any wound dressing, referred to as the 'control group'.

We photographed the wound healing progress over 21 days and presented it in Figs. S15 and S16 Fig. 9a. Each experimental group exhibited a progressive decrease in the size of the open wound on days 7, 14, and 21. Notably, we did not administer antibiotics to any group. Visually, there were no signs of excessive redness, irritation, or infection in the animals.

Some animals managed to remove their dressings and occasionally broke pieces off the silicone splints. In these instances, we re-sutured the broken splints at each dressing change until day 14. By the end of the 14th day, the wounds had significantly healed (as seen in Fig. 9a), eliminating the need for splints to prevent skin contraction. Consequently, we chose not to replace them thereafter. If an animal removed its bandage and removed the dressing, we replaced them.. Importantly, we observed no significant impact on wound healing in animals that either removed their bandages or broke their splints, likely due to the absence of infection.

Replacing the PZ and PTBA hydrogel wound dressings was a straightforward process. We could easily separate the hydrogel from the wound without any difficulties. In comparison, the PZ and PTBA dressings could be effortlessly removed using an isotonic serum wash, unlike the positive control Kaltostat®, which adhered strongly to the wound bed and impeded new skin formation. The transparency of the PZ and PTBA hydrogel films facilitated easy monitoring of the wound healing process.

The data displayed in Fig. 9b indicates a normal distribution for all measured variables, as confirmed by the Shapiro-Wilk test. We present these results as mean values along with their standard deviations. In all groups, macroscopic analysis showed a significant reduction in wound size from the day of surgery to the final evaluation at 21 days. This reduction is indicative of neoepithelialization and the replacement of damaged tissue with new tissue, as illustrated in Fig. 9. It's worth noting that superficial wounds often heal naturally through physiological mechanisms when left untreated, as referenced in studies [124,125]. However, patient non-compliance and the risk of secondary infections can adversely affect healing rates, particularly in the treatment of deep wounds, chronic conditions, or burns. Thus, accelerating the healing process is crucial to mitigate post-wound complications, as suggested in a study [126].

By day 14 of wounding and dressing, notable macroscopic differences were observed among the groups (as shown in Fig. 9a and Fig. S16). Measurements taken on the 7th and 14th days revealed that the control, PTBA, and PZ groups achieved better wound closure compared to the Kaltostat® group, as documented in Fig. 9a, Fig. S16, and Tables S9, S10, and S11.

When analyzing the median wound closure area and the interquartile range (IQR) values of the groups over time, we observed that the control

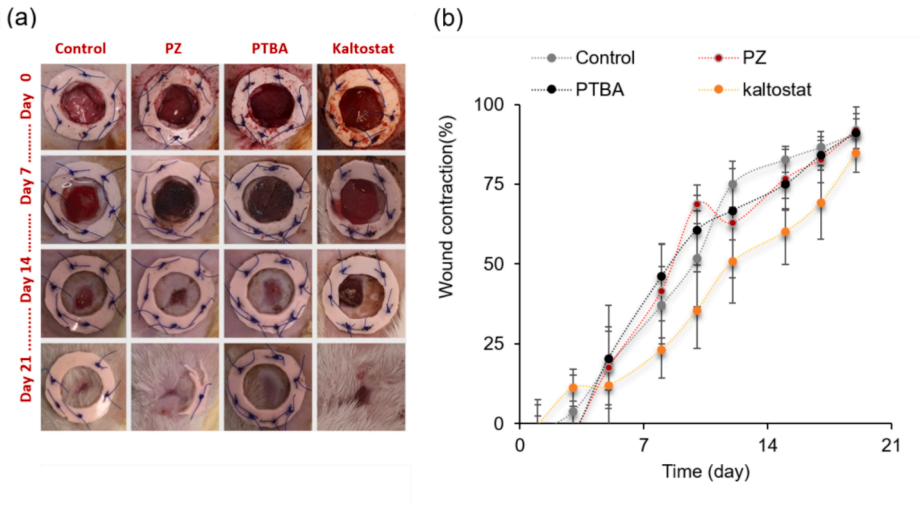

Fig. 9. (a) Photographs of wound treated Control, PZ, PTBA, Kaltostat® groups on 0, 7, 14 and 21 days of post wounding, (b) Wound healing rate with different treatments.

group exhibited a decrease after day 14, while the PZ group showed the highest median value on day 21 (as seen in, Fig. S16, and Table S10). The exceptionally high IQR value (21.5) in the control group during the first week can likely be attributed to the animals' varied immune responses. Generally, the deviations from the median were larger, which could be due to differences in the animals' behaviors.

On the final day of treatment, the PZ group exhibited the highest percentage of wound closure at 91.89% ± 7.3, as detailed in Table S9. This was closely followed by the PTBA group at 91.02% ± 6.0, the control group at 90.88% ± 4.7, and the Kaltostat group at 84.8% ± 6.2. Notably, the highest rates of wound closure per day (wound closure area/day) were achieved by the PZ group (4.72) and the PTBA group (4.62) on day 21, outperforming both the control group (4.2) and the Kaltostat group (4.05) with statistical significance ($p < 0.05$) (Table S11). Additionally, the efficacy of the healing process was further validated by the emergence of hair follicles in the treated wounds [127].

When comparing the wound closure time in our study groups to those in previous studies on wound dressings, as cited in studies [128,129], our results show a relatively rapid closure rate. By day 21, the wound sizes in our study were comparable to those reported in earlier research. However, it's important to note that we used splints to prevent skin contraction and spontaneous closure, a necessary step due to the presence of the panniculus carnosus muscle in the dorsal area of rats, as discussed in studies [130,131]. This methodology yields more realistic and comparable results to what might be expected in human wound dressings, as indicated in a study [132]. It's conceivable that the closure percentages might have been even higher if the use of splints had been omitted.

3.13. Histological analysis of hydrogel wound dressings

Wound healing is a dynamic process that can be divided into three phases as: inflammation, proliferation, and maturation, respectively. The process is not linear and often wounds can progress both forwards and back through the phases depending upon intrinsic and extrinsic forces at work within the case [133,134].

The inflammatory phase is morphologically characterized by a predominance of neutrophils and macrophages. Since samples were taken on the 21st day, no morphological sign representing this stage could be observed. During proliferation, the wound is 'rebuilt' with new granulation tissue, which is comprised of collagen and extracellular matrix, and into which a new network of blood vessels develops. Epithelial cells finally resurface the wound, a process known as 'epithelialization'.

Epithelialization is vital in wound healing, during which, several types of cytokeratins are expressed in different stages of this process [135]. Stratification and keratinization were accomplished in all groups on the 21st day of healing. Immune staining intensity of both cytokeratin-16, one of the markers expressed in basal cells during the initial period of epithelialization, and cytokeratin 10, a marker indicating keratinocyte differentiation in the suprabasal layers are prominent in the control group, while staining is weak to moderate in the PZ, PTBA and Kaltostat® groups (Figs. 10 and 11). This finding may relate to the early stabilization of keratinocyte proliferation and differentiation as a consequence of enhanced and moist wound healing due to the dressing material [136].

Maturation is the final phase and occurs once the wound has closed. This phase involves remodeling of collagen from type III to type I. The samples from all groups were taken presumably in the maturation phase. The abundance of mature (type I) collagen fibers is highest in PZ, PTBA, and Kaltostat® groups, respectively, compared to the control group in which immature (type III) collagen fibers were prominent. This result is consistent with the enhanced healing process associated with the dressings used in the study (Figs. 12 and 13). Cellular activity reduces, and the number of blood vessels in the wounded area regresses and decreases in the late maturation phase [137]. Vascular structures stained with the CD-31 antibody were observatory less in the control group and more abundant in Kaltostat® group, while the differences were insignificant (Fig. 14). Nevertheless, the relative difference may relate to fluctuating rate of healing among groups and hence is a reflection of different stages of the maturation phase.

CD-68 is used as a marker for macrophages in the healing tissue (Fig. 15). The activity of macrophages is expected to decrease in the late stages of healing due to the remodeling of the wound. Subtle differences in the late phases of healing may result from the composition of dressings interacting with stroma which may have a critical role in chronic wound healing [138].

4. Conclusion

In conclusion, our study presents the successful development of two distinct pectin-based multifunctional hydrogel formulations utilizing either zeolite or TBA through a straightforward sol–gel method. Our *in silico* analysis explored the complex molecular interactions among these components, revealing a complex interplay. The subsequent comprehensive *in vitro* evaluations demonstrated the hydrogels' remarkable stability, biodegradability, porous structure, self-healing properties, antioxidant and hemostatic capabilities, antibacterial efficacy, and biocompatibility. We performed a deep rheological analysis in order to

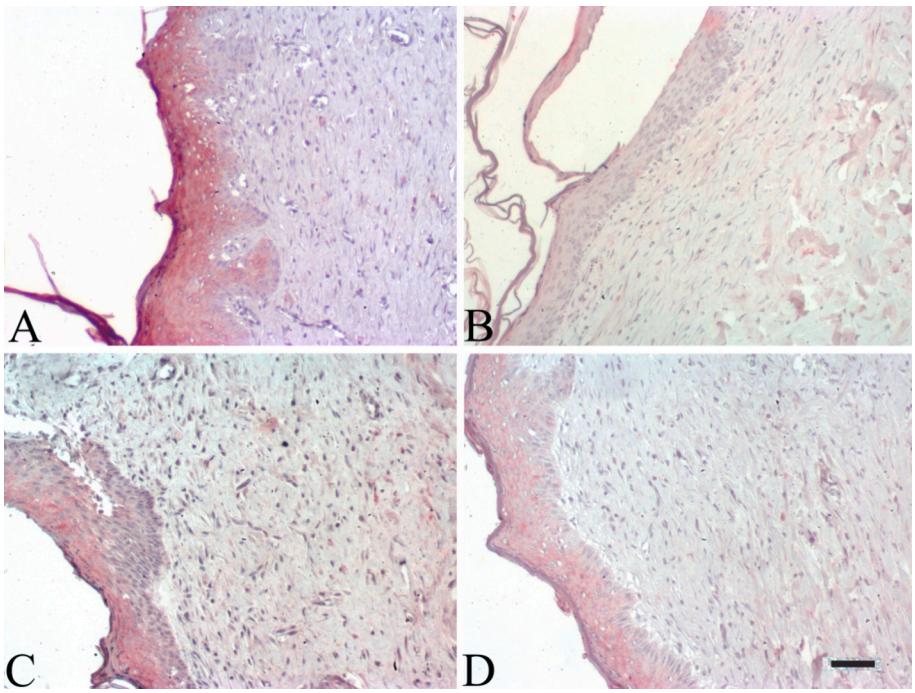

Fig. 10. Immune histochemical staining of cytokeratin16 in epidermal cells. In control group (A), strong immune staining reaction are observed. Immune staining intensity is moderate and comparable in Kaltostat®, PTBA and PZ groups (B, C and D respectively). Scalebar 50 μm.

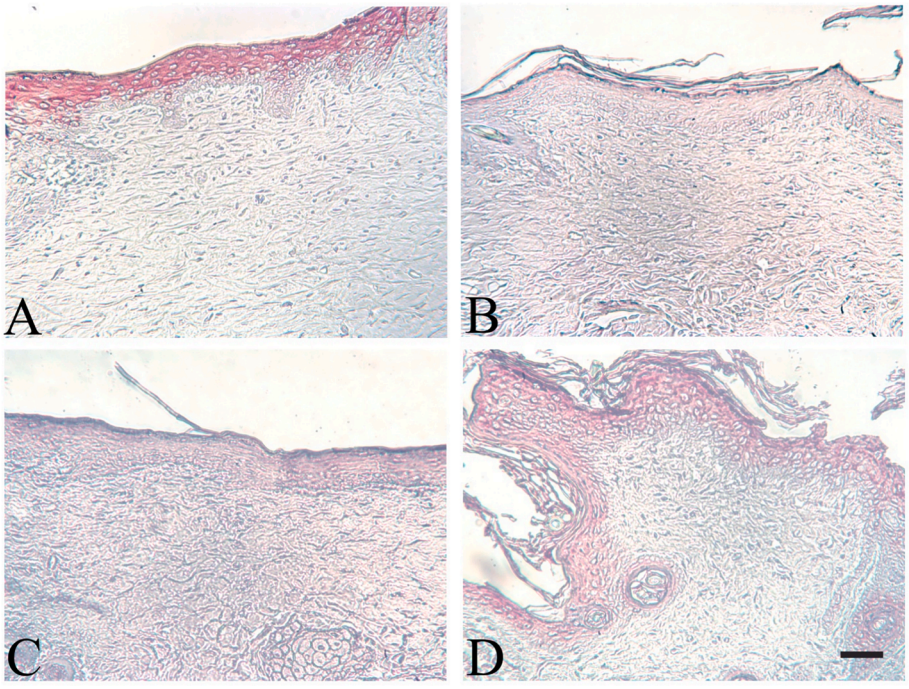

Fig. 11. Immune histochemical staining of cytokeratin-10 in epidermal cells. In control group (A), strong immue staining reaction are observed; In Kaltostat® group (B) intensity of staining is low and moderate in PTBA and PZ groups (C and D respectively). Scalebar 50 μm.

describe the function-structural relationship. This research not only advances the field of multifunctional wound dressings but also represents a significant contribution to polyscahharide science literature, with *in silico, in vitro*, and *in vivo* methods. Our investigation, employing comprehensive full-thickness skin wound models, has revealed that PZ and PTBA hydrogel dressings are capable of accelerating the wound healing process and enhancing tissue regeneration. Notably, the highest rate of wound closure was observed in the group treated with the PZ group. This finding is demonstrating the therapeutic potential of PZ formulations.

Another critical component of our study was the detailed histological examination conducted during the maturation phase, also known as the remodeling phase, of wound healing. Here, we observed a prevalence of mature (type I) collagen fibers in the groups treated with PZ and PTBA, in contrast to the control group, which predominantly exhibited immature (type III) collagen fibers. This observation underscores the

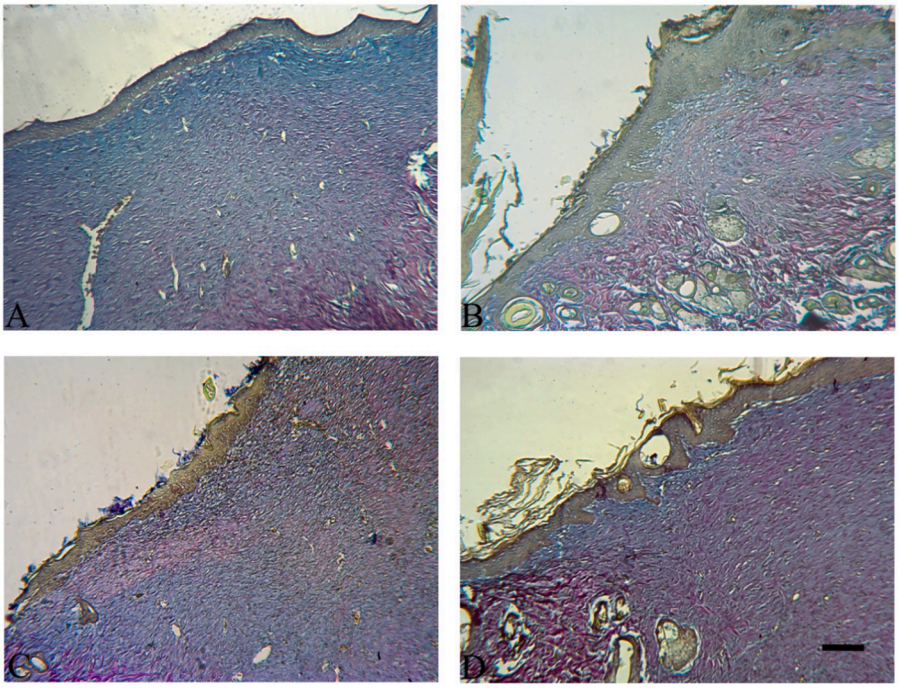

Fig. 12. Micrographs of A. Control, B. Kaltostat®, C. PTBA, D. PZ groups. Immature (blue) and mature (red) collagen fibers can be visualized by Herovici staining. Scalebar 150 μm.

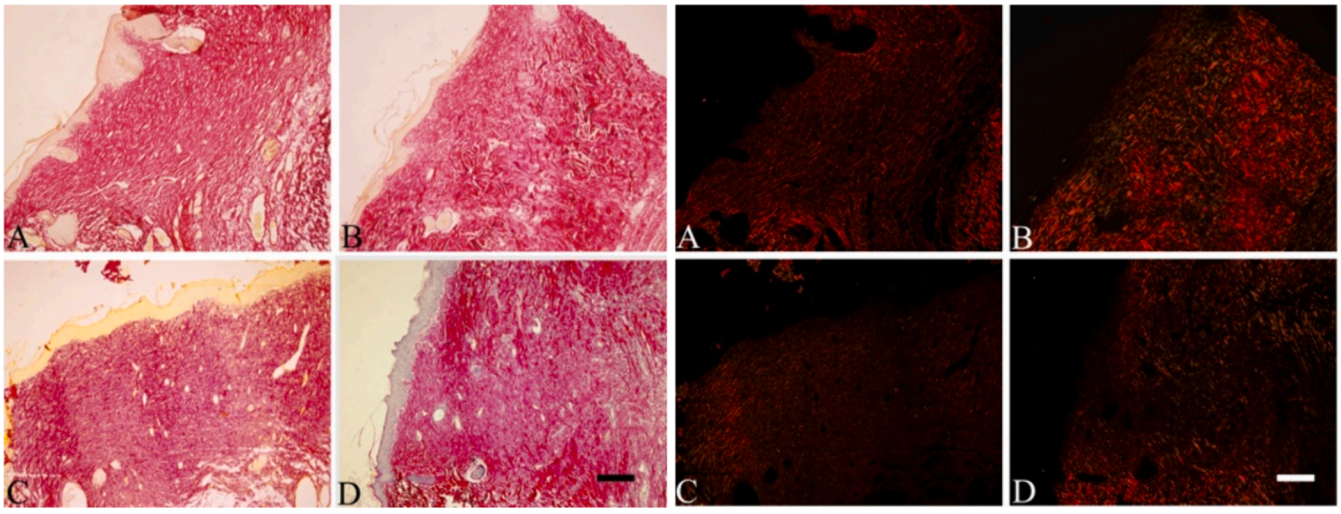

Fig. 13. Micrographs of the preparations stained with picro-sirius dye, were taken with a light microscope on the left and a polarized microscope on the right. Mature collagen fibers are seen as red bundles in the micrographs taken with the polarized microscope on the right. Reticular fibers and immature collagen fibrils are seen as green blots. Scalebar: 100 μm.

efficacy of our hydrogel formulations in supporting and advancing the critical processes inherent in the maturation phase of wound healing.

The reason for these observations may be due to; (i) the superior properties of pectin polymer in wound healing [139,140], (ii) antioxidant capacity of the TBA molecule, (iii) high oxygen permeability of the zeolite particles [17], (iv) the high structural integrity of the PTBA formulation, (v) shear thinning and pH-dependent adhesion properties of PZ and PTBA hydrogels that impart to the structures self-healing capabilities and facilitate filling and sealing of cavities and irregular edges, providing a moist interface that might facilitate cell mmigration and signaling as a scaffold for fibroblasts, (vi) antibacterial property of pectin hydrogel, (vii) the long term controlled delivery of PC molecules that have bacteriostatic, bactericidal, fungistatic, or fungicidal properties against a variety of microorganisms such as *Enterococcus faecalis, Escherichia coli, Pseudomonas aeruginosa, Borrelia spp*, and S. aureus [42–44,141] and cell membrane modulation, increasing resistance to infection and toxins, antioxidant activity, neuron regeneration, and reducing carpal tunnel syndrome [46].

All these findings highlight that these hydrogels hold great potential in clinical applications as multifunctional wound dressing materials.

5. Materials and methods

5.1. Molecular dynamics simulations

The three-dimensional structures of 2-thiobarbituric acid (TBA)

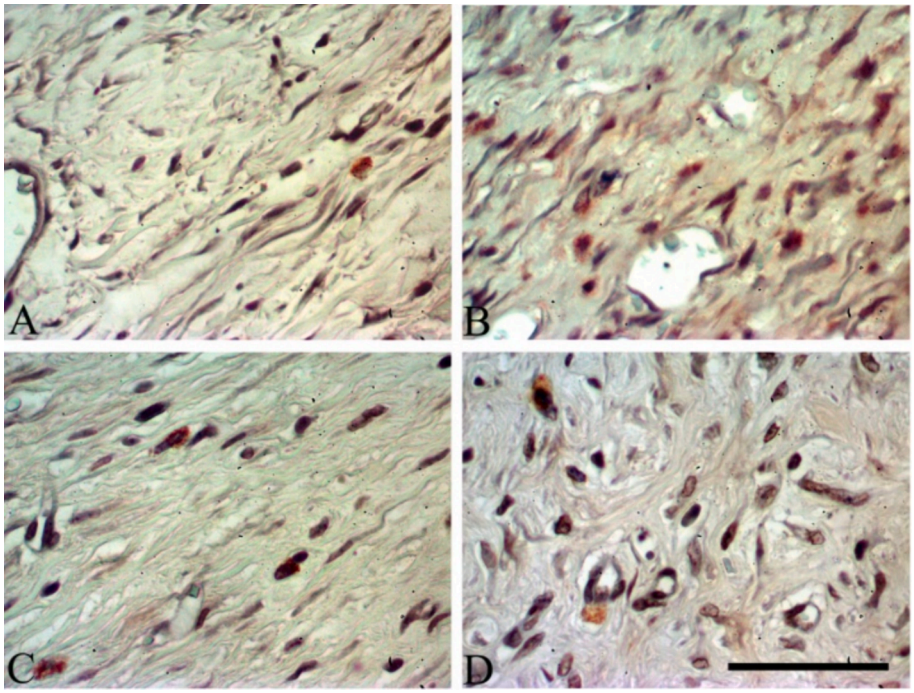

Fig. 14. Immunohistochemical staining of CD31 for endothelial cells showing immun-positive cells (red) in A. Control, B. Kaltostat®, C. PTBA, D. PZ groups. 40x. Scalebar: 50 μm.

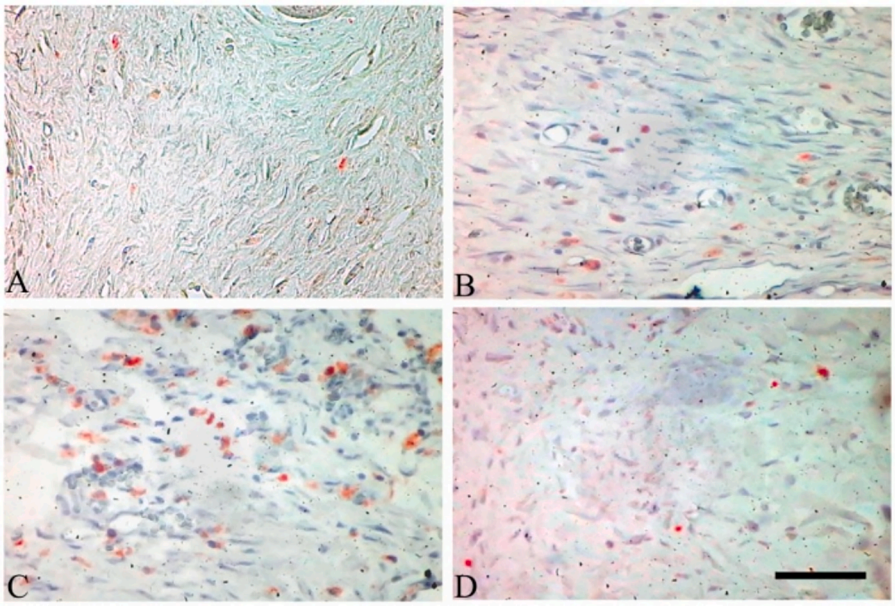

Fig. 15. Immunohistochemical staining of CD68 in control, Kaltostat®, PTBA, and PZ groups respectively. Scalebar: 50 μicrons.

(Fig. S1a) and procaine (PC) (Fig. S1b) were downloaded from the Zinc Database [142]. Both molecules were protonated according to the experimental conditions. Geometric optimizations of the PC and TBA molecules were carried out with Gauss 5.0 [143] using the B3LYP approach of the 6–31 + G** basis set. To parameterize the systems for molecular dynamics (MD), the CHARMM force field was utilized through CHARMM-GUI [144]. Preparing the systems for MD simulations involved using PyMol and VMD interfaces [145,146].

Since the majority of pectin chains are composed of linear poly-galacturonic acid (PGAL) forms, galacturonic acid (GAL) monomers with deprotonated carboxyl groups were created to mimic the experimental conditions (Fig. 16). Two linear, 21-unit long oligo-galacturonic acid chains were modeled using Glycan Reader [145] and placed 10 Å apart using PyMol. Ca^{2+} ions were randomly distributed between the chains to maintain an egg-box configuration. Additionally, 5 TBA molecules for the TGAL model and both 5 TBA and 5 PC molecules for the PTGAL model were randomly placed approximately 3–15 Å apart from the PGAL chains. The details of the two systems studied are listed in Table 1.

The simulation boxes were solvated with TIP3P water using 20 Å padding and neutralized to a physiological salt concentration of 150 mM by randomly adding Na^{+} and Cl^{-} ions. The systems' energy was

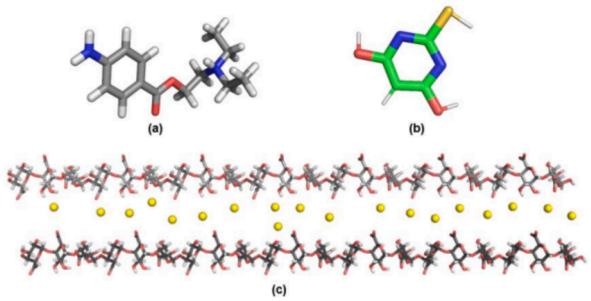

Fig. 16. Geometrically minimized structures. (a) Protonated procaine, (b) Protonated TBA (c) cross-linked PGAL chains. Structures are shown in the sticks and in CPK coloring. Ca2+ are shown as yellow spheres in (c).

minimized to remove any steric clashes, using 5000 steps of a conjugate gradient with a tolerance of 0.01 kcal/mol. Following energy minimization, the systems underwent equilibration under NPT (constant number of particles, constant pressure, constant temperature) conditions for a duration of 10 ps at 300 K. Subsequently, a 200 ns long NVT (constant number of particles, constant volume, constant temperature) simulation was employed, where temperature was controlled by the Nose−Hoover thermostat [147], and pressure was controlled by the Langevin barostat [148]. Non-bonded interactions were cut off at 12 Å, and the Periodic Electrostatic Particle Mesh method [149] was used for electrostatic interactions. Total simulation time was set as 200 ns with a time step of 2 fs while using the SHAKE algorithm [150]. The CHARMM_all36 force field [144,151] was utilized for both energy minimization and molecular dynamics (MD) simulations, with the NAMD 2.7 package serving as the computational tool [152].

The dynamic behaviors of PGAL and PTGAL models were analyzed, focusing on root mean square deviation (RMSD), the radius of gyration (Rg), end to end distance (Rn). RMSD of the modeled chains is one of the critical parameters illustrating the particle's position's deviation relative to their reference position at each time (Equation (1)).

$$RMSD = \sqrt{\frac{1}{N}\sum_{i=1}^{N}\left(r_i^X - r_i^Y\right)^2} \quad (1)$$

Here, *ri* is the position of atom *i* in the structurally aligned structures *X* and *Y*, and *N* is the total number of equivalent atoms. The initial structure of the NVT production run is used as the reference (*Y*) structure.

The calculation of the radius of gyration (Rg) and end-to-end distances analysis (Rn) provide insight into the degree of compactness and the time required for structural and conformational equilibrium [153].

$$R_g^2 = \frac{\sum_{i=1}^{N} m_i d_i^2}{\sum_{i=1}^{N} m_i} \quad (2)$$

Where *mi* is the atomic weight, and *di* is the distance between I^{th} atom and the center of mass. To determine significant non-bonded interactions, the radial distribution function (g(r)) of selected atom pairs or groups is examined.

6. Experimental section

6.1. Materials

Amidated LM pectin was provided by Herbstrith & Fox company (Neuenbürg, Germany). Glycerol (purity-99%) and $CaCl_2{\cdot}2H_2O$ were purchased from Labkim (Istanbul, Turkey). TRIS (2-amino-2-(hydroxymethyl) propane-1,3-diol), procaine HCl and 2-thiobarbituric acid were supplied by Sigma-Aldrich (Düsseldorf, Germany). Sodium silicate (Merck, Darmstadt, Germany), granular sodium aluminate (Riedel-de Haen, Bucharest, Romania), and NaOH pellets (Carlo Erba, Val-de Reuil, France) were purchased for the zeolite synthesis. All chemicals were of analytical grade and were not further purified. Double deionized water was used throughout the experiments.

6.2. Zeolite-A synthesis

Zeolite-A, each measuring 2–3 μm in size, was synthesized with a molar composition of 3.165 Na_2O:1 Al_2O_3:1.926 SiO_2:128 H_2O in Na form (NaA) from a gel-type reaction mixture [154]. The synthesis was carried out in an oven at 99 °C for 3.5 h in a polypropylene vessel. Sodium silicate, granular sodium aluminate, NaOH pellets, and de-ionized water were utilized as reagents.

6.2.1. Preparation of PZ and PTBA hydrogels

Zeolite-added (PZ) and 2-thiobarbituric acid added (PTBA) hydrogels were fabricated through a host–guest interaction with $CaCl_2$ as the cross-linker and glycerol as the plasticizer. PZ hydrogels were prepared based on diffusion into a membrane-controlled system. Initially, we dehydrated zeolite particles, which served as a reservoir for procaine molecules, at 120 °C under vacuum overnight. Subsequently, we mixed the zeolite-procaine suspension (30 mg drug at pH 9.1 / 30 mg zeolite). We stirred it for 24 h at room temperature and 100 rpm in a dark environment to immobilize PC to zeolite particles. The concentration of the immobilized drug was measured at 289.9 nm using a LAMBDA 1050 UV/Vis Spectrophotometer. Next, we prepared a pectin-glycerol solution (600 mg pectin/300 mg glycerol in ultra-deionized water) and stirred it for two hours at 150 rpm. We added the procaine-loaded zeolite suspension to the pectin-glycerol solution and stirred it for another 24 h at room temperature and 150 rpm. Finally, we poured the suspension onto 70 mg CaCl2 solution in a Petri plate and left it to gel spontaneously for 24 h on an orbital shaker at 27 ± 1 °C, resulting in the dry hydrogel.

For the PTBA hydrogels, we followed a similar process. Initially, we mixed 30 mg of TBA molecules in a TRIS buffer solution at pH 6.4 with the pectin-glycerol solution. Subsequently, we gently added the procaine solution at pH 9.1 to the hydrogel film. The hydrogel film with procaine was left on a magnetic stirrer for an additional 24 h under the same conditions to ensure complete adsorption. Finally, the PTBA hydrogel was dried.

6.3. Rheological behavior of hydrogels

Rheological analyses were conducted using an Anton Paar Physica MCR 301 rheometer (Anton Paar, Graz, Austria) equipped with a plate temperature-controlled base (Viscotherm VT2) and a hood using a PP25 measuring plate. Throughout the measurements, the samples were tightly sealed to prevent any material loss, and a solvent trap was used to prevent solvent evaporation from the samples. The dynamic measurements included amplitude sweep, frequency sweep, thixotropy analysis, creep and recovery, and stress relaxation. The experimental setup is detailed in Table S5.

Strain sweep tests, ranging from 0.1% to 1000% of storage modulus (G') and loss modulus (G'') at 1 Hz and 25° were carried out to evaluate (i) the Linear viscoelastic (LVE) region or critical strain, (ii) (γ_L), the elastic modulus at the critical strain (G'_{LVE}), and (iii) the flow point (γ_f, G_f).

Frequency sweep tests were conducted over a range of 0.1 to 100 rad/s to determine the storage modulus (G'), loss modulus (G''), and loss factor (damping factor; tan δ) within the LVE range.

To assess the rapid self-healing capability of the cross-linked wet PZ and PTBA hydrogels, we conducted an oscillation strain test at 25°C. The test was performed using a 25 mm parallel plate geometry with a 1 mm gap. The procedure involved six cycles, beginning with a low strain of 1% applied for 1 min, followed by a high strain of 1000% for 1 min to

complete one cycle.

We applied a 25 Pa shear stress for 300 s (creep phase) for the creep tests, and then released it. We allowed the hydrogels to recover their strain for an additional 600 s (recovery phase) and recorded the strain as a function of time during both phases.

Stress relaxation tests were conducted at four different temperatures (25, 35, 45, and 60°C) to investigate the temperature dependence of the hydrogel's characteristic relaxation time (τ). PTBA and PZ hydrogels were first equilibrated at the set temperature for 15 min, and 1% strain is applied. The relaxation modulus was monitored over time, and the characteristic time (τ) was defined as the time to reach 1/e (37%) of the initial stress.

6.4. Visual inspection of the self-healing property of the hydrogels

PZ and PTBA hydrogels were shaped into circle-shaped samples for visual inspection, one of which was stained with a dye for better visual inspection. The self-healing process was conducted by cutting two semi-circular pieces from a single sample and re-joining them after 15 min. The re-joined hydrogels were then stored at 25°Cin for 10 min to allow for self-healing, resulting in PZ and PTBA self-healed hydrogels. When the hydrogels dried, a hole was punched in the middle, and a 50 g weight was attached to the middle of the hydrogel.

6.5. In vitro drug release

The *in vitro* drug release of PTBA and PZ hydrogel films was evaluated in TRIS buffer at pH 6.4. To carry out this evaluation, equal-diameter drug-loaded pectin (P), PTBA and PZ hydrogel disks were placed in vials containing buffer solution and are stirred on an orbital shaker at 25 ± 1 °C. The drug release is monitored with a UV/Vis Spectrophotometer (Perkin Elmer Corp, Waltham, MA, USA) specifically at a wavelength of 289.9 nm. Throughout the duration of the experiment, samples were periodically collected using a 900 μL pipette. Upon collection, the absorbance of each sample was measured, and the solution was promptly returned to its respective vial to maintain consistency in the testing environment. The use of the pure pectin (P) hydrogel served as a baseline control. This control was essential to verify at 289.9 nm whether any degradation products from the pectin hydrogel itself could potentially interfere with the absorbance readings of the drug-loaded PTBA and PZ hydrogels, as detailed in the Supplementary (Fig. S12). For accurate determination of the drug concentration, Lambert–Beer's law was employed [155].

6.6. In vitro drug release kinetic

PC release kinetics from PZ and PTBA hydrogels was investigated via linear fitting of five kinetic models: Zero-order, First-order, Higuchi, Korsmeyer-Peppas, and Hixson-Crowell (Table 4). Finally, each graph of the model was plotted, and the R^2 value determined the most appropriate fitted model.

6.7. Swelling degree

To determine the swelling degree, the equal-sized circular pieces of hydrogel specimens were cut from the dry film. These samples were then immersed in 25 ml of pH 6.4 TRIS buffer solution in a Petri dish, kept at room temperature. At specific intervals, the samples were removed from the Petri dish, weighed, and then placed back into the buffer solution. To ensure accurate measurements, any excess moisture on the sample surface was carefully removed by placing it between two sheets of filter paper before each weight measurement. The swelling ratio is calculated using the Equation (3).

$$\text{Swelling Ratio} = \frac{Ws - W_d}{W_d} \tag{3}$$

Where *Ws* and *Wd* are the weights of the swelled and dry samples, respectively.

6.8. In vitro characterization of the hydrogels as wound dressing material

Flexibility, mean mass per unit area ($g.m^{-2}$), and thickness (mm) of hydrogel films are tested, as well as fluid handling capacities, dehydration rate, dispersion characteristics, and pH shifting capacity of wound dressings [160,161] and compared to those of commercial dressing Kaltostat® (Table S4). The flexibility of PZ and PTBA hydrogels was measured by the D522-93a [162] standard test methods for mandrel bend test of attached organic coatings, American Society for Testing and Materials (ASTM) using an Erichsen Model 266S cylindrical mandrel bending tester [162]. The apparatus contains 14 stainless steel mandrels from 2 to 32 mm in diameter. The smallest cylinder diameter is reported when a sample does not show cracking or flaking after bending (Table S4). Mass per unit area ($g.m^{-2}$) and thickness (mm) of hydrogel films are determined according to BS EN 12127:1998 [163] and BS EN ISO 9073-2:1997 [164], respectively (Table S4). The hydrogels' absorbency or fluid handling behavior is measured according to BS EN 137261:2002 [165] test methods. The salt solution for the measurement (2.298 g NaCl and 0.368 g $CaCl_2{\cdot}2H_2O$ in 1 L of de-ionized water) was prepared. 5 cm × 5 cm sized PZ and PTBA samples are weighed (W2) and placed in a Petri plate. The Petri is placed in an incubator at 37 ± 1°C for 30 min, and the salt solution at 37 ± 1°C is added to the Petri with a ratio of 1:40 (w/v). After 30 min, hydrogel films were removed from the incubator and weighed. Before each weighing, excess moisture on the sample surface is removed by gently placing the film between two filter sheets. The absorbency ratio was calculated as the mass loss by using Equation (4).

$$\text{Mass loss upon drying}\,(g.g^{-1}) = \frac{W_1 - W_2}{W_2} \tag{4}$$

W_1 and W_2 are the weights of the hydrogel film before and after the test, respectively.

To determine the dehydration rate of the PZ and PTBA hydrogel films (5 cm × 5 cm), they were dried for 24 h at 37 ± 1°C in an incubator before the test. They are immersed in de-ionized water for 30 min at 37 ± 1°C. After 30 min, they were removed from the incubator and weighed (W_1) [166]. The samples were then re-dried for 24 h at 37 ± 1°C and re-weighed (W_2). Before each measurement, excess moisture on the sample surface was removed by gently placing the film between two filter sheets. Dehydration rate (g.min-^{1}) was calculated by,

$$\text{Dehydration rate}\,(g\,.min^{-1}) = \frac{W_1 - W_2}{T} \tag{5}$$

Dispersion characteristics of the dressings were watched following the standard BS EN 13726-2:2001 test methods for primary wound dressings [167]. First, the 5 cm × 5 cm square-shaped hydrogel film dressings were immersed in a 250 mL conical flask with 50 ± 1 mL of the salt solution described above. After that, the flask is slowly swirled for 60 s without causing a vortex, and the dispersion of the sample was visually determined and photographed.

The effect of the presence of the hydrogel films on the pH of the external solution was examined in de-ionized water at a ratio of 1:100 (w/v) at room temperature [161]. The pH was measured after 3 h and 24 h using WTW—Portable pH meters.

6.9. Blood clothing test

Whole bovine blood was collected from the slaughterhouse and stored in citrate tubes. The punched hydrogel films (5 mm in diameter) were swelled in PBS for 15 min, and samples are placed in a centrifuge tube. 40 μL of whole blood containing sodium citrate were slowly added

into the tube. Coagulation was initiated by adding 3 μL of 0.2 M $CaCl_2$ solution. The tubes are kept in a 37°C incubator until the pre-set time point; 1 mL of water was slowly pipetted to dissolve unbound blood and simultaneously avoid disturbing the clot. The absorbance of the supernatant was measured at 540 nm using an ELISA reader (BMG LABTECH SPECTROstar® Nano). The blood-clotting index (BCI) is calculated using the following Equation:

$$\text{BCI}\,(\%) = \frac{A}{B} x100\% \quad (6)$$

Where A represents the absorbance of hydrogel samples, and B represents the reference value [168]. A higher BCI value indicates a lower level of hemostatic effect.

6.10. Antioxidant activity test

The antioxidant properties of hydrogel films were investigated with α,α-diphenyl-picrylhydrazyl (DPPH) free radical scavenging method, following a protocol with slight modifications [169–171]. Circular hydrogel films were prepared using a 5 mm biopsy punch. The hydrogel films were soaked in 1 mL of methanol and vortexed. After 90 min of incubation at 37°C in the dark, 1 mL of 200 mM DPPH solution was mixed with 1 mL of extract solution and incubated for 30 min at room temperature in the dark. The antioxidant properties of hydrogel films were determined by spectrophotometric measuring the absorbance at 515 nm against control after 30 min at room temperature using an ELISA reader (BMG LABTECH SPECTROstar® Nano). The scavenging activity on DPPH radicals was calculated using the following formula:

$$\text{DPPH Scavenging}\,(\%) = \frac{A_{control} - A_{sample}}{A_{control}} x100 \quad (7)$$

$A_{control}$ represents the absorbance of the DPPH solution in methanol at 517 nm, and A_{sample} represents the absorbance of the samples with DPPH solution at 517 nm.

6.11. In vitro cell viability assay

The effects of the samples on the cell viability were assessed using the WST-1 cell proliferation assay (Roche, Mannheim, Germany), following the manufacturer's prescribed procedure. Initially, PCS-201–012 human dermal fibroblast cells (ATCC) were seeded into a 96-well tissue culture plate at a density of 5 × 103 cells/well and were cultured at 37°C in a humidified atmosphere with 5% CO_2 for 24 h for attachment of the cells. Subsequently, the medium was removed and replenished with 300 μL fresh medium. Two mg of samples were placed into each well. After 24 h of incubation, the medium and the samples were removed and replaced with 100 μL of fresh culture medium and 10 μL of WST-1 reagent. The absorbance of formazan crystals was measured at 450 nm using a microplate reader (Molecular Devices, CA, USA). The absorbance values of the treated groups were presented as a percentage of the absorbance versus the control group. Triplicates of samples were used in each experiment, and three independent experiments were performed. The results were analyzed with a one-way analysis of variance (ANOVA) followed by the Bonferroni post hoc test using SPSS version 13.0 (SPSS, Chicago, IL, USA).

6.12. Anti-bacterial analysis

Overnight cultures of E. coli ATCC® 25922™ and S. aureus ATCC® 29213™ in Mueller-Hinton broth were used to prepare bacterial suspensions within the same broth. The turbidity of these suspensions was adjusted to the 0.5 McFarland turbitidy standart, corresponding to a concentration of 1–2 × 108 CFU/mL, using spectrophotometric measurements. Both suspensions were inoculated on Mueller-Hinton agar plates using an automated plate inoculator. Hydrogels (P, PZ, and PTA) were applied (5 mm in diameter) on the surface of bacteria-inoculated Mueller-Hinton agar plates. Ampicillin-containing paper disks (2 μg and 10 μg) were used as controls for S. aureus and E. coli, respectively. Plates were incubated at 37 °C for 24 h, and growth inhibition zones around disks were measured for antibacterial activity evaluation.

6.13. In vivo Animal experiments

Animal experiments were carried out with the standard ethical guidelines approved by Animal Experiments Center Ethics Committee (Turkey) and the Koc University Local Ethics Committee of Animal Experiments approves the experiment methodology. Thirty-two adult male Wistar rats, weighing 380–410 g, were given ad libitum access to commercial food and water.

The experiment was divided into four groups: control, PTBA, PZ, and Kaltostat®. Anesthesia was induced through an intraperitoneal injection of Xylazine HCl (Alfazyne 2%, Alfasan International B.V., Holland) (3 mg/kg) and Ketamine HCl (Alfamine 10%, Alfasan International B.V., Holland) (75 mg/kg) and maintained with inhalation of isoflurane. Pain management is achieved through subcutaneous administration of Meloxicam (Metacam, Boehringer Ingelheim, Germany) (1 $mg.kg^{-1}$) on days 0, 2, 4, 7, and 9.

The dorsal skin of the rats was shaved, and a full-thickness 16 mm punch biopsy was taken from the dorsolateral side under sterile conditions. The wound dressings were prepared by punching to a diameter of 20 mm and sterilized with UV before the operations. Silicone splints (Manufacturer: Silicone MYS 301, Baltalı Silicone Rubber Industry and Trade. Ltd. Sti. Çerkezköy, Tekirdag) were prepared from the silicone sheet by punch cutting with an inner diameter of 1.6 cm and an outer diameter of 2.5 cm and sterilized with UV before operations. The wound dressings were placed over the wound and fixed around the skin with six sutures. The edge of the dressing was left under the skin [172]. The skin on the outer side of the splints was disinfected with baticone. Sterile gauze was placed over the splint and body of the rats are covered with medical plaster (Fig. S13). Antibiotics were not given to the rats for more objective results.

Bandage changes were performed on days 0, 2, 4, 7, 9, 11, 14, 16, 18, and 21. Photographing was administered on days 0, 7, 14, and 21 days. Animals are anesthetized with isoflurane using an induction chamber and mask for these procedures. On the 9th and 11th days, wounds were washed superficially with polygyl (brand) for preventive purposes. During bandage changes, the PTBA, PZ, and Kaltostat® dressings on the wound area were moistened with an isotonic solution, and the bandages were renewed. PTBA, PZ, and Kaltostat ® dressings have adhered to the bandage or removed by the animals and were prepared again with sterile spare dressings, according to the size of the wound, and placed on the wound area. The skin outside the splint was cleaned with baticon at each bandage renewal. On day 21, the rats were euthanized and a 2.5 cm wide, 4 cm long skin sample was taken and placed in formaldehyde-filled containers, leaving the wound area in the middle.

6.13.1. Calculating wound healing rate

Wounds were photographed at predetermined time, following a specific schedule. The photos were taken in a standardized method from a height of 15 cm. The wound surface areas were analyzed using *ImageJ Software*. All measurements are made in triplicate. The wound reduction ratio over time was calculated using the formula described by as Giusto et al. described [173].

$$\text{Wound area reduction rate}\,(\text{warr}) = \frac{A_t}{A_0} x100 \quad (8)$$

A_0 is the area of the wound on day 0. A_t is the area of the wound on the specified day.

6.14. Histochemistry

Biopsies were fixed with 10% buffered formaldehyde solution, passed through a series of ascending alcohol and embedded in paraffin blocks. Sections with a thickness of 2.5–3 μm were evaluated by histochemical and immunohistochemical methods.

Histochemical staining: Herovici and Picro-Sirius stains showed collagen maturation levels in granulation tissue of each group. Sections were evaluated using bright field and polarized microscopes.

6.15. İmmunohistochemistry

Sections were kept at 56°C for 1 night and then treated with toluol for 30 min for deparaffinization. They were passed through the descending alcohol series (100, 90, 70%) for dehydration and thenwere taken into distilled water. To block endogenous peroxidase activity, sections were kept in 5% hydrogen peroxide solution for 15 min in the dark. For antigen retrieval, sections were heated in a microwave pH 6.0 citrate buffer three times for 5 min and were washed again with phosphate buffer. After 5 min of incubation with UltraV block (Ultravision anti-polyvalent kit, (Thermo Scientific)), the sections were incubated with CD-68 (ab125212; 1:200), CD31 (Santa Cruz sc-365804; 1:100), cytokeratin-16 (Santa Cruz sc-53255; 1:100) and cytokeratin-10 (Santa Cruz sc-23877; 1:500) primary antibodies at +4°C overnight. Sections were then incubated with secondary antibody, streptavidin biotin solution, and AEC chromogen (Thermo Scientific) for 10 min, respectively. Counter staining was done with Mayer hematoxylin.

Sections were sealed with water based medium were evaluated by three histologists with light microscope (Olympus OM45, Japan).

6.16. Statistical analysis

Data were analyzed with the Shapiro-Wilk test to evaluate the normality and statistical differences were disclosed using one-way ANOVA for parametric values. Statistical significance was set at $p < 0.05$. All tests are performed using IBM SPSS Statistics 27 software.

CRediT authorship contribution statement

Banu Kocaağa: Writing – review & editing, Writing – original draft, Visualization, Software, Resources, Project administration, Methodology, Investigation, Funding acquisition, Formal analysis, Data curation, Conceptualization. **Yetkin Öztürk:** Writing – original draft, Methodology, Formal analysis, Data curation, Conceptualization. **H. Ceren Kurçin:** Formal analysis. **Ö. Zeynep Güner-Yılmaz:** Methodology, Investigation, Formal analysis, Conceptualization. **Ozge Kurkcuoglu:** Writing – review & editing, Supervision, Software, Methodology, Investigation. **Melkon Tatlier:** Methodology, Investigation, Formal analysis. **İlkay Özdemir:** Writing – original draft, Formal analysis, Data curation, Conceptualization. **Elif Kervancioglu Demirci:** Writing – original draft, Visualization, Methodology, Investigation, Formal analysis, Data curation, Conceptualization. **Tuğba Kotil:** Writing – original draft, Visualization, Methodology, Investigation, Formal analysis, Data curation, Conceptualization. **Seyhun Solakoğlu:** Writing – review & editing, Validation, Supervision, Resources, Methodology, Investigation, Formal analysis, Data curation, Conceptualization. **Burak Aksu:** Methodology, Investigation, Data curation, Conceptualization. **Saime Batirel:** Methodology, Formal analysis, Data curation, Conceptualization. **Ayça Bal-Öztürk:** Writing – original draft, Methodology, Formal analysis, Data curation. **F. Seniha Güner:** Writing – review & editing, Writing – original draft, Validation, Supervision, Resources, Project administration, Methodology, Investigation, Formal analysis, Data curation, Conceptualization.

Declaration of competing interest

The authors declare the following financial interests/personal relationships which may be considered as potential competing interests: Banu Kocaaga reports financial support was provided by Scientific and Technological Research Council of Turkey. If there are other authors, they declare that they have no known competing financial interests or personal relationships that could have appeared to influence the work reported in this paper.

Data availability

Data will be made available on request.

Acknowledgment

This study was funded by the Scientific and Technological Research Council of Turkey (TUBITAK) ARDEB 1002 Grant No 120M370.

Appendix A. Supplementary data

Supplementary data to this article can be found online at https://doi.org/10.1016/j.eurpolymj.2024.113280.

References

[1] C.K. Sen, Human wound and its burden: Updated 2020 compendium of estimates, Adv. Wound Care 10 (5) (2021) 281–292, https://doi.org/10.1089/wound.2021.0026.
[2] B. Bhar, D. Chouhan, N. Pai, B.B. Mandal, Harnessing multifaceted next-generation technologies for improved skin wound healing, ACS Appl. Bio Mater. 4 (11) (2021) 7738–7763, https://doi.org/10.1021/acsabm.1c00880.
[3] Z. Yang, et al., Highly stretchable, adhesive, biocompatible, and antibacterial hydrogel dressings for wound healing, Adv. Sci. 8 (8) (2021) 1–12, https://doi.org/10.1002/advs.202003627.
[4] H.M. Nguyen, T.T. Ngoc Le, A.T. Nguyen, H.N. Thien Le, T.T. Pham, Biomedical materials for wound dressing: recent advances and applications, RSC Adv. 13 (8) (2023) 5509–5528, https://doi.org/10.1039/d2ra07673j.
[5] G. Mahmodi, et al., From microporous to mesoporous mineral frameworks: An alliance between zeolite and chitosan, Carbohydr. Res. 489 (February) (2020), https://doi.org/10.1016/j.carres.2020.107930.
[6] S. Wu, B. Chen, Q. Ye, Blood compatible chitin composite nanofibrous microspheres as efficient adsorbents for removal of blood ammonia in hyperammonemia, Microporous Mesoporous Mater. 343 (May) (2022), https://doi.org/10.1016/j.micromeso.2022.112137.
[7] A. Kabir, A. Sarkar, A. Barui, Acute and chronic wound management: Assessment, therapy and monitoring strategies, Regen. Med. (2023) 97–125.
[8] P.A. Markov, N.S. Krachkovsky, E.A. Durnev, E.A. Martinson, S.G. Litvinets, S. V. Popov, Mechanical properties, structure, bioadhesion, and biocompatibility of pectin hydrogels, J. Biomed. Mater. Res. - Part A 105 (9) (2017) 2572–2581, https://doi.org/10.1002/jbm.a.36116.
[9] F. Munarin, et al., Pectin-based injectable biomaterials for bone tissue engineering, Biomacromolecules 12 (3) (2011) 568–577, https://doi.org/10.1021/bm101110x.
[10] M. Jridi, O. Abdelhedi, A. Salem, H. Kechaou, M. Nasri, Y. Menchari, Physicochemical, antioxidant and antibacterial properties of fish gelatin-based edible films enriched with orange peel pectin: Wrapping application, Food Hydrocoll. 103 (July) (2019) 2020, https://doi.org/10.1016/j.foodhyd.2020.105688.
[11] L. Chang, et al., Self-healing hydrogel based on polyphosphate-conjugated pectin with hemostatic property for wound healing applications, Biomater. Adv. 139 (May) (2022) 212974, https://doi.org/10.1016/j.bioadv.2022.212974.
[12] F.O. Ogutu, T.H. Mu, Ultrasonic degradation of sweet potato pectin and its antioxidant activity, Ultrason. Sonochem. 38 (2017) 726–734, https://doi.org/10.1016/j.ultsonch.2016.08.014.
[13] A. Sivashanmugam, R. Arun Kumar, M. Vishnu Priya, S.V. Nair, R. Jayakumar, An overview of injectable polymeric hydrogels for tissue engineering, Eur. Polym. J. 72 (2015) 543–565, https://doi.org/10.1016/j.eurpolymj.2015.05.014.
[14] S. Soltani, R. Emadi, S.H. Javanmard, M. Kharaziha, A. Rahmati, Shear-thinning and self-healing nanohybrid alginate-graphene oxide hydrogel based on guest-host assembly, Int. J. Biol. Macromol. 180 (2021) 311–323, https://doi.org/10.1016/j.ijbiomac.2021.03.086.
[15] Y. Shitrit, M. Davidovich-Pinhas, H. Bianco-Peled, Shear thinning pectin hydrogels physically cross-linked with chitosan nanogels, Carbohydr. Polym. 225 (July) (2019), https://doi.org/10.1016/j.carbpol.2019.115249.
[16] H. Chen, B. Chiou, Y. Wang, and D. A. Schiraldi, "Biodegradable Pectin/Clay Aerogels," 2013.

[17] A.B. Kocaaga, O. Kurkcuoglu, M. Tatlier, S. Batirel, F.S. Guner, Low-methoxyl pectin–zeolite hydrogels controlling drug release promote in vitro wound healing, J. Appl. Polym. Sci. 136 (24) (2019) 1–16, https://doi.org/10.1002/app.47640.
[18] M. Nasrollahzadeh, M. Sajjadi, S. Iravani, R.S. Varma, Starch, cellulose, pectin, gum, alginate, chitin and chitosan derived (nano)materials for sustainable water treatment: A review, Carbohydr. Polym. 251 (September 2020) (2021) 116986, https://doi.org/10.1016/j.carbpol.2020.116986.
[19] M.A. Fischbach, C.T. Walsh, Antibiotics for emerging pathogens, Science 325 (5944) (2009) 1089–1093, https://doi.org/10.1126/science.1176667.
[20] V. Urias-Orona, J. Huerta-Oros, E. Carvajal-Millán, J. Lizardi-Mendoza, A. Rascón-Chu, A.A. Gardea, Component analysis and free radicals scavenging activity of cicer arietinum L. husk pectin, Molecules 15 (10) (2010) 6948–6955, https://doi.org/10.3390/molecules15106948.
[21] Z. Wang, D. Luo, Antioxidant activities of different fractions of polysaccharide purified from Gynostemma pentaphyllum Makino, Carbohydr. Polym. 68 (1) (2007) 54–58, https://doi.org/10.1016/j.carbpol.2006.07.022.
[22] S. Guo, et al., One-step synthesis of multifunctional chitosan hydrogel for full-thickness wound closure and healing, Adv. Healthc. Mater. 11 (4) (2022) 1–19, https://doi.org/10.1002/adhm.202101808.
[23] L. Li, B. Yan, J. Yang, L. Chen, H. Zeng, Novel mussel-inspired injectable self-healing hydrogel with anti-biofouling property, Adv. Mater. 27 (7) (2015) 1294–1299, https://doi.org/10.1002/adma.201405166.
[24] M. Tatlier, C. Atalay-Oral, A. Bayrak, T. Maraş, A. Erdem, Impact of ion exchange on zeolite hydrophilicity/hydrophobicity monitored by water capacity using thermal analysis, Thermochim. Acta 713 (May) (2022), https://doi.org/10.1016/j.tca.2022.179240.
[25] C. Nomicisio, et al., Natural and synthetic clay minerals in the pharmaceutical and biomedical fields, Pharmaceutics 15 (5) (2023), https://doi.org/10.3390/pharmaceutics15051368.
[26] M. Tatlier, Ç. Atalay-Oral, Crystallization of zeolite a coatings from natural zeolite, Mater. Res. 19 (6) (2016) 1469–1477, https://doi.org/10.1590/1980-5373-MR-2016-0564.
[27] Ç. Atalay-Oral, Ş. Bora, M. Tatlier, Effects of using different polymers in post-synthesis treatments of zeolite a coatings, Chem. Eng. Commun. 202 (3) (2015) 375–383, https://doi.org/10.1080/00986445.2013.840826.
[28] Z. Dagli, C. Atalay-Oral, C. Tasdelen-Yucedag, M. Tatlier, How may preferential heating of the substrate aid template-free preparation of EMT zeolite and its coatings? Microporous Mesoporous Mater. 337 (October 2021) (2022) 111905 https://doi.org/10.1016/j.micromeso.2022.111905.
[29] P. Zarrintaj, et al., Zeolite in tissue engineering: Opportunities and challenges, MedComm 1 (1) (2020) 5–34, https://doi.org/10.1002/mco2.5.
[30] L. Bacakova, M. Vandrovcova, I. Kopova, I. Jirka, Applications of zeolites in biotechnology and medicine-a review, Biomater. Sci. 6 (5) (2018) 974–989, https://doi.org/10.1039/c8bm00028j.
[31] S. Pourshahrestani, E. Zeimaran, I. Djordjevic, N.A. Kadri, M.R. Towler, Inorganic hemostats: The state-of-the-art and recent advances, Mater. Sci. Eng. C 58 (2016) 1255–1268, https://doi.org/10.1016/j.msec.2015.09.008.
[32] S.M. Mortazavi, A. Atefi, P. Roshan-Shomal, N. Raadpey, G. Mortazavi, Development of a novel mineral based haemostatic agent consisting of a combination of bentonite and zeolite minerals, J. Ayub Medical College, Abbottabad: JAMC 21 (1) (2009) 3–7.
[33] N. Ninan, M. Muthiah, I.K. Park, T.W. Wong, S. Thomas, Y. Grohens, Natural polymer/inorganic material based hybrid scaffolds for skin wound healing, Polym. Rev. 55 (3) (2015) 453–490, https://doi.org/10.1080/15583724.2015.1019135.
[34] H. Ipek, M. Avci, N. Aydilek, M. Yerturk, The effect of zeolite on oxidant/antioxidant status in healthy dairy cows, Acta Vet. Brno 81 (1) (2012) 43–47, https://doi.org/10.2754/avb201281010043.
[35] N.I. Yarovan, Effect of zeolites on adaptation processes in cows, Russ. Agric. Sci. 34 (2) (2008) 120–122, https://doi.org/10.3103/s106836740802016x.
[36] B. Kocaaga, O. Kurkcuoglu, M. Tatlier, G. Dinler-Doganay, S. Batirel, F.S. Güner, Pectin–zeolite-based wound dressings with controlled albumin release, Polymers 14 (3) (2022), https://doi.org/10.3390/polym14030460.
[37] T. Ceyhan, M. Tatlier, H. Akçakaya, In vitro evaluation of the use of zeolites as biomaterials: Effects on simulated body fluid and two types of cells, J. Mater. Sci. - Mater. Med. 18 (8) (2007) 1557–1562, https://doi.org/10.1007/s10856-007-3049-y.
[38] D. Van Der Spoel, E. Lindahl, B. Hess, G. Groenhof, GROMACS: Fast, flexible, and free, J. Comput. Chem. 26 (16) (2005) 1701–1718, https://doi.org/10.1002/jcc.20291.
[39] A. Sharma, et al., Exploiting the thiobarbituric acid scaffold for antibacterial activity, ChemMedChem 13 (18) (2018) 1923–1930, https://doi.org/10.1002/cmdc.201800414.
[40] G. Kaur, P. Gupta, K. Harjai, V. Singh, Synthesis of new thiobarbituric acid derived spiroheterobicyclic compounds and their antimicrobial activity, Drug Dev. Res. 75 (3) (2014) 202–210, https://doi.org/10.1002/ddr.21172.
[41] O.Z. Güner, B. Kocaaga, S. Batirel, O. Kurkcuoglu, F.S. Güner, 2-Thiobarbituric acid addition improves structural integrity and controlled drug delivery of biocompatible pectin hydrogels, Int. J. Polym. Mater. Polym. Biomater. 70 (10) (2021) 703–711, https://doi.org/10.1080/00914037.2020.1760272.
[42] S.M. Johnson, B.E. Saint John, A.P. Dine, Local anesthetics as antimicrobial agents: A review, Surg. Infect. (Larchmt.) 9 (2) (2008) 205–213, https://doi.org/10.1089/sur.2007.036.
[43] A.M. Parr, D.E. Zoutman, J.S.D. Davidson, Antimicrobial activity of lidocaine against bacteria associated with nosocomial wound infection, Ann. Plast. Surg. 43 (3) (1999) 239–245, https://doi.org/10.1097/00000637-199909000-00003.
[44] L. Schorter, R.K. Straubinger, Impact of four local anaesthetics on growth and viability of in vitro cultured Borrelia burgdorferi sensu stricto, Borrelia bavariensis and Borrelia afzelii, Ticks Tick-borne Dis. 12 (5) (2021) pp, https://doi.org/10.1016/j.ttbdis.2021.101735.
[45] A. Akcal, S. Karsidag, K. Yildiz, N. Yesiloglu, M. Akcal, F. Kabukcuoglu, The effects of locally applied procaine on wound healing, Arch. Clin. Exp. Surg. (ACES) 4 (1) (2015) 41, https://doi.org/10.5455/aces.20140606054447.
[46] Ö. Karadaş, F. Tok, Ü.H. Ulaş, Z. Odabaşi, The effectiveness of triamcinolone acetonide vs. procaine hydrochloride injection in the management of carpal tunnel syndrome: A double-blind randomized clinical trial, Am. J. Phys. Med. Rehabil. 90 (4) (2011) 287–292, https://doi.org/10.1097/PHM.0b013e31820639ec.
[47] X. Zhao, et al., Synthesis of dual functional procaine-derived carbon dots for bioimaging and anticancer therapy, Nanomedicine 15 (7) (2020) 677–689, https://doi.org/10.2217/nnm-2019-0390.
[48] A. Wu Chuang, O. Kepp, G. Kroemer, L. Bezu, Direct cytotoxic and indirect, immune-mediated effects of local anesthetics against cancer, Front. Oncol. 11 (January) (2022) 1–14, https://doi.org/10.3389/fonc.2021.821785.
[49] O.I. Efimova, A.I. Dimitrieva, O.P. Nesterova, A.V. Aldyakov, A.V. Obukhova, T. N. Ivanova, Methods for the effective treatment of animal burns, IOP Conf. Ser.: Earth Environ. Sci. 346 (1) (2019), https://doi.org/10.1088/1755-1315/346/1/012057.
[50] N. Mielenz, G. Möbius, I. Steinhöfel, and W. Baumgartner, "Einfluss eines multimodalen Schmerz - managements sowie des Alters zum Zeitpunkt des Eingriffes auf die Wundheilung nach thermischer Zerstörung der Hornanlage bei weiblichen," pp. 836–850, 2021.
[51] B. Ying, H. Huang, H. Li, M. Song, S. Wu, H. Ying, Procaine inhibits proliferation and migration and promotes cell apoptosis in osteosarcoma cells by upregulation of MicroRNA-133b, Oncol. Res. 25 (9) (2017) 1463–1470, https://doi.org/10.3727/096504017x14878518291077.
[52] Y.C. Li, Y. Wang, D.D. Li, Y. Zhang, T.C. Zhao, C.F. Li, Procaine is a specific DNA methylation inhibitor with anti-tumor effect for human gastric cancer, J. Cell. Biochem. 119 (2) (2018) 2440–2449, https://doi.org/10.1002/jcb.26407.
[53] B. Kocaaga, F.S. Guner, O. Kurkcuoglu, Molecular dynamics simulations can predict the optimum drug loading amount in pectin hydrogels for controlled release, Mater. Today Commun. 31 (February) (2022) 103268, https://doi.org/10.1016/j.mtcomm.2022.103268.
[54] J. Martínez-Sabando, F. Coin, J.H. Melillo, S. Goyanes, S. Cerveny, A review of pectin-based material for applications in water treatment, Materials 16 (6) (2023), https://doi.org/10.3390/ma16062207.
[55] L. Cao, W. Lu, A. Mata, K. Nishinari, Y. Fang, Egg-box model-based gelation of alginate and pectin: A review, Carbohydr. Polym. 242 (April) (2020) 116389, https://doi.org/10.1016/j.carbpol.2020.116389.
[56] G.P. Raeber, M.P. Lutolf, J.A. Hubbell, Molecularly engineered PEG hydrogels: A novel model system for proteolytically mediated cell migration, Biophys. J. 89 (2) (2005) 1374–1388, https://doi.org/10.1529/biophysj.104.050682.
[57] B. Jachimska, A. Pajor, Physico-chemical characterization of bovine serum albumin in solution and as deposited on surfaces, Bioelectrochemistry 87 (2012) 138–146, https://doi.org/10.1016/j.bioelechem.2011.09.004.
[58] K. Matyjaszewski, M. Möller, Polycondensation Polym. Sci. 5 (2013).
[59] A. Gasperini, et al., Characterization of hydrogen bonding formation and breaking in semiconducting polymers under mechanical strain, Macromolecules 52 (6) (2019) 2476–2486, https://doi.org/10.1021/acs.macromol.9b00145.
[60] F.J. Galindo-Rosales, F.J. Rubio-Hernandez, Static and dynamic yield stresses of aerosil® 200 suspensionsin polypropylene glycol, Appl. Rheol. 20 (2) (2010) 1–10, https://doi.org/10.3933/ApplRheol-20-22787.
[61] J. Park, S. Bin Park, S.M. Yang, W.H. Hong, C.R. Choi, J.H. Kim, Rheological characterization and optimization of gelled electrolyte for sealed lead-acid batteries by small amplitude dynamic oscillation measurement, J. Non Cryst. Solids 351 (27–29) (2005) 2352–2357, https://doi.org/10.1016/j.jnoncrysol.2005.05.023.
[62] S. Rooj, A. Das, K.W. Stöckelhuber, D.Y. Wang, V. Galiatsatos, G. Heinrich, Understanding the reinforcing behavior of expanded clay particles in natural rubber compounds, Soft Matter 9 (14) (2013) 3798–3808, https://doi.org/10.1039/c3sm27519a.
[63] J. Yang, C.R. Han, Dynamics of silica-nanoparticle-filled hybrid hydrogels: Nonlinear viscoelastic behavior and chain entanglement network, J. Phys. Chem. C 117 (39) (2013) 20236–20243, https://doi.org/10.1021/jp404616s.
[64] S. Lin-Gibson, H.J. Walls, S.B. Kennedy, E.R. Welsh, Reaction kinetics and gel properties of blocked diisocyinate crosslinked chitosan hydrogels, Carbohydr. Polym. 54 (2) (2003) 193–199, https://doi.org/10.1016/S0144-8617(03)00159-0.
[65] B. Nystrom, H. Walderhaug, F.K. Hansen, Rheological behavior during thermoreversible gelation of aqueous mixtures of ethyl(hydroxyethy1)cellulose and surfactants, Langmuir 11 (1995) 750–757.
[66] P. Alaee, M. Kamkar, M. Arjmand, Fumed silica-based suspensions for shear thickening applications: A full-scale rheological study, Langmuir 38 (16) (2022) 5006–5019, https://doi.org/10.1021/acs.langmuir.2c00591.
[67] Y. Liang, Z. Li, Y. Huang, R. Yu, B. Guo, Dual-dynamic-bond cross-linked antibacterial adhesive hydrogel sealants with on-demand removability for post-wound-closure and infected wound healing, ACS Nano 15 (4) (2021) 7078–7093, https://doi.org/10.1021/acsnano.1c00204.
[68] K. Sahajpal, et al., Dynamic protein and polypeptide hydrogels based on Schiff base co-assembly for biomedicine, J. Mater. Chem. B 10 (17) (2022) 3173–3198, https://doi.org/10.1039/d2tb00077f.

[69] A.I. Cernencu, A.I. Dinu, I.C. Stancu, A. Lungu, H. Iovu, Nanoengineered biomimetic hydrogels: A major advancement to fabricate 3D-printed constructs for regenerative medicine, Biotechnol. Bioeng. 119 (3) (2022) 762–783, https://doi.org/10.1002/bit.28020.
[70] H. Qin, T. Zhang, N. Li, H.P. Cong, S.H. Yu, Anisotropic and self-healing hydrogels with multi-responsive actuating capability, Nat. Commun. 10 (1) (2019) 1–11, https://doi.org/10.1038/s41467-019-10243-8.
[71] H.A. Barnes, Q.D. Nguyen, Rotating vane rheometry-a review, J. Nonnewton. Fluid Mech. 98 (1) (2001) 1–14, https://doi.org/10.1016/S0377-0257(01)00095-7.
[72] J. Mewis, N.J. Wagner, Thixotropy, Adv. Colloid Interface Sci. 147–148 (C) (2009) 214–227, https://doi.org/10.1016/j.cis.2008.09.005.
[73] B. Zhang, J. He, M. Shi, Y. Liang, B. Guo, Injectable self-healing supramolecular hydrogels with conductivity and photo-thermal antibacterial activity to enhance complete skin regeneration, Chem. Eng. J. 400 (June) (2020), https://doi.org/10.1016/j.cej.2020.125994.
[74] M.H. Zainol, R.K. Shuib, The effect of ionic cross linker on Self-healing natural rubber, AIP Conf. Proc. 2267 (September) (2020), https://doi.org/10.1063/5.0016182.
[75] N.A. Sirajuddin, M.S.M. Jamil, M.A.S.M. Lazim, Effect of cross-link density and the healing efficiency of self-healing poly(2-hydroxyethyl methacrylate) hydrogel, E-Polymers 14 (4) (2014) 289–294, https://doi.org/10.1515/epoly-2014-0036.
[76] D. Li, S. Wang, Y. Meng, Z. Guo, M. Cheng, J. Li, Fabrication of self-healing pectin/chitosan hybrid hydrogel via Diels-Alder reactions for drug delivery with high swelling property, pH-responsiveness, and cytocompatibility, Carbohydr. Polym. 268 (March) (2021), https://doi.org/10.1016/j.carbpol.2021.118244.
[77] T.C. Brito-Oliveira, I.C.F. Moraes, S.C. Pinho, O.H. Campanella, Modeling creep/recovery behavior of cold-set gels using different approaches, Food Hydrocolloids 123 (August 2021) (2022) 107183, https://doi.org/10.1016/j.foodhyd.2021.107183.
[78] E. Krempl, F. Khan, Rate (time)-dependent deformation behavior: An overview of some properties of metals and solid polymers, Int. J. Plast 19 (7) (2003) 1069–1095, https://doi.org/10.1016/S0749-6419(03)00002-0.
[79] H.A. Jiménez-Avalos, E.G. Ramos-Ramírez, J.A. Salazar-Montoya, Viscoelastic characterization of gum arabic and maize starch mixture using the Maxwell model, Carbohydr. Polym. 62 (1) (2005) 11–18, https://doi.org/10.1016/j.carbpol.2005.07.007.
[80] N. Sozer, Rheological properties of rice pasta dough supplemented with proteins and gums, Food Hydrocoll. 23 (3) (2009) 849–855, https://doi.org/10.1016/j.foodhyd.2008.03.016.
[81] S. Gulyuz, Y. Yagci, B. Kiskan, Exploiting the reversible covalent bonding of boronic acids for self-healing/recycling of main-chain polybenzoxazines, Polym. Chem. 13 (24) (2022) 3631–3638, https://doi.org/10.1039/d2py00068g.
[82] Y. Chen, Z. Tang, X. Zhang, Y. Liu, S. Wu, B. Guo, Covalently cross-linked elastomers with self-healing and malleable abilities enabled by boronic ester bonds, ACS Appl. Mater. Interfaces 10 (28) (2018) 24224–24231, https://doi.org/10.1021/acsami.8b09863.
[83] J. Siepmann, N.A. Peppas, Modeling of drug release from delivery systems based on hydroxypropyl methylcellulose (HPMC), Adv. Drug Deliv. Rev. 64 (SUPPL) (2012) 163–174, https://doi.org/10.1016/j.addr.2012.09.028.
[84] O.Z. Güner, B. Kocaaga, S. Batirel, O. Kurkcuoglu, F.S. Güner, 2-Thiobarbituric acid addition improves structural integrity and controlled drug delivery of biocompatible pectin hydrogels, Int. J. Polym. Mater. Polym. Biomater. (2020), https://doi.org/10.1080/00914037.2020.1760272.
[85] D.Y. Arifin, L.Y. Lee, C.H. Wang, Mathematical modeling and simulation of drug release from microspheres: Implications to drug delivery systems, Adv. Drug Deliv. Rev. 58 (12–13) (2006) 1274–1325, https://doi.org/10.1016/j.addr.2006.09.007.
[86] P. Zare, et al., Alginate sulfate-based hydrogel/nanofiber composite scaffold with controlled Kartogenin delivery for tissue engineering, Carbohydr. Polym. 266 (April) (2021), https://doi.org/10.1016/j.carbpol.2021.118123.
[87] X. Huang, C.S. Brazel, On the importance and mechanisms of burst release in matrix-controlled drug delivery systems, J. Control. Release 73 (2–3) (2001) 121–136, https://doi.org/10.1016/S0168-3659(01)00248-6.
[88] M.C. Berg, L. Zhai, R.E. Cohen, M.F. Rubner, Controlled drug release from porous polyelectrolyte multilayers, Biomacromolecules 7 (1) (2006) 357–364, https://doi.org/10.1021/bm050174e.
[89] D. Shi, et al., Photo-cross-linked scaffold with kartogenin-encapsulated nanoparticles for cartilage regeneration, ACS Nano 10 (1) (2016) 1292–1299, https://doi.org/10.1021/acsnano.5b06663.
[90] M.M. Pakulska, et al., Encapsulation-free controlled release: Electrostatic adsorption eliminates the need for protein encapsulation in PLGA nanoparticles, Sci. Adv. 2 (5) (2016) pp, https://doi.org/10.1126/sciadv.1600519.
[91] M. Servatan, et al., Zeolites in drug delivery: Progress, challenges and opportunities, Drug Discov. Today 25 (4) (2020) 642–656, https://doi.org/10.1016/j.drudis.2020.02.005.
[92] S. Rodoplu, et al., Dual effect of procaine-loaded pectin hydrogels: pain management and in vitro wound healing, Polym. Bull. (2020), https://doi.org/10.1007/s00289-020-03210-7.
[93] O.Z. Güner, C. Cam, B. Arabacioglu-Kocaaga, S. Batirel, F.S. Güner, Theophylline-loaded pectin-based hydrogels. I. Effect of medium pH and preparation conditions on drug release profile, J. Appl. Polym. Sci. 135 (38) (2018) pp, https://doi.org/10.1002/app.46731.
[94] P. Toews, J. Bates, Influence of drug and polymer molecular weight on release kinetics from HEMA and HPMA hydrogels, Sci. Rep. 13 (1) (2023) 1–9, https://doi.org/10.1038/s41598-023-42923-3.
[95] E.P. Da Silva, et al., Drug release profile and reduction in the in vitro burst release from pectin/HEMA hydrogel nanocomposites crosslinked with titania, RSC Adv. 6 (23) (2016) 19060–19068, https://doi.org/10.1039/c5ra27865a.
[96] P.L. Ritger, N.A. Peppas, A simple equation for description of solute release II. Fickian and anomalous release from swellable devices, J. Control. Release 5 (1) (1987) 37–42, https://doi.org/10.1016/0168-3659(87)90035-6.
[97] S.A. Shah, et al., Curcumin-laden hyaluronic acid-co-Pullulan-based biomaterials as a potential platform to synergistically enhance the diabetic wound repair, Int. J. Biol. Macromol. 185 (June) (2021) 350–368, https://doi.org/10.1016/j.ijbiomac.2021.06.119.
[98] N. Ajaz, et al., Pectin-based hydrogels with adjustable properties for controlled delivery of nifedipine: development and optimization, Polym. Bull. 77 (11) (2020) 6063–6083, https://doi.org/10.1007/s00289-019-03065-7.
[99] M. Pandey, et al., Budesonide-loaded pectin/polyacrylamide hydrogel for sustained delivery: Fabrication, characterization and in vitro release kinetics, Molecules 26 (9) (2021) 1–13, https://doi.org/10.3390/molecules26092704.
[100] S. Groult, S. Buwalda, T. Budtova, Pectin hydrogels, aerogels, cryogels and xerogels: Influence of drying on structural and release properties, Eur. Polym. J. 149 (February) (2021), https://doi.org/10.1016/j.eurpolymj.2021.110386.
[101] Y. Wang, et al., Chitosan-bound carboxymethylated cotton fabric and its application as wound dressing, Carbohydr. Polym. 221 (December 2018) (2019) 202–208, https://doi.org/10.1016/j.carbpol.2019.05.082.
[102] K. Quan, G. Li, L. Tao, Q. Xie, Q. Yuan, X. Wang, Diaminopropionic acid reinforced graphene sponge and its use for hemostasis, ACS Appl. Mater. Interfaces 8 (12) (2016) 7666–7673, https://doi.org/10.1021/acsami.5b12715.
[103] Z. Chen, et al., A rapid hemostatic sponge based on large, mesoporous silica nanoparticles and: N -alkylated chitosan, Nanoscale 10 (43) (2018) 20234–20245, https://doi.org/10.1039/c8nr07865c.
[104] R. Pereira, A. Carvalho, D.C. Vaz, M.H. Gil, A. Mendes, P. Bártolo, Development of novel alginate based hydrogel films for wound healing applications, Int. J. Biol. Macromol. 52 (1) (2013) 221–230, https://doi.org/10.1016/j.ijbiomac.2012.09.031.
[105] L.C. Xu, M.E. Meyerhoff, C.A. Siedlecki, Blood coagulation response and bacterial adhesion to biomimetic polyurethane biomaterials prepared with surface texturing and nitric oxide release, Acta Biomater. 84 (2019) 77–87, https://doi.org/10.1016/j.actbio.2018.11.035.
[106] M. Bagheri, M. Validi, A. Gholipour, P. Makvandi, E. Sharifi, Chitosan nanofiber biocomposites for potential wound healing applications: Antioxidant activity with synergic antibacterial effect, Bioeng. Transl. Med. (August) (2021) 1–15, https://doi.org/10.1002/btm2.10254.
[107] A. Bermúdez-Oria, G. Rodríguez-Gutiérrez, E. Rodríguez-Juan, A. González-Benjumea, J. Fernández-Bolaños, Molecular interactions between 3,4-dihydroxyphenylglycol and pectin and antioxidant capacity of this complex in vitro, Carbohydr. Polym. 197 (May) (2018) 260–268, https://doi.org/10.1016/j.carbpol.2018.05.089.
[108] M. Naziroğlu, Molecular role of catalase on oxidative stress-induced Ca2 signaling and TRP cation channel activation in nervous system, J. Recept. Signal Transduction 32 (3) (2012) 134–141, https://doi.org/10.3109/10799893.2012.672994.
[109] Y. Xue, et al., Safranal, an active constituent of saffron, ameliorates myocardial ischemia via reduction of oxidative stress and regulation of Ca^{2+} homeostasis, J. Pharmacol. Sci. 143 (3) (2020) 156–164, https://doi.org/10.1016/j.jphs.2020.03.005.
[110] S. Park, J.A. Imlay, High levels of intracellular cysteine promote oxidative DNA damage by driving the Fenton reaction, J. Bacteriol. 185 (6) (2003) 1942–1950, https://doi.org/10.1128/JB.185.6.1942-1950.2003.
[111] A. Chetouani, et al., Multifunctional hydrogels based on oxidized pectin and gelatin for wound healing improvement, Int. J. Biol. Macromol. 212 (May) (2022) 248–256, https://doi.org/10.1016/j.ijbiomac.2022.05.082.
[112] M. Gabriele, C. Gerardi, J.J. Lucejko, V. Longo, L. Pucci, V. Domenici, Effects of low sulfur dioxide concentrations on bioactive compounds and antioxidant properties of Aglianico red wine, Food Chem. 245 (November 2017) (2018) 1105–1112, https://doi.org/10.1016/j.foodchem.2017.11.060.
[113] E.E. Battin, J.L. Brumaghim, Antioxidant activity of sulfur and selenium: A review of reactive oxygen species scavenging, glutathione peroxidase, and metal-binding antioxidant mechanisms, Cell Biochem. Biophys. 55 (1) (2009) 1–23, https://doi.org/10.1007/s12013-009-9054-7.
[114] M. Valko, C.J. Rhodes, J. Moncol, M. Izakovic, M. Mazur, Free radicals, metals and antioxidants in oxidative stress-induced cancer, Chem. Biol. Interact. 160 (1) (2006) 1–40, https://doi.org/10.1016/j.cbi.2005.12.009.
[115] E. Mukwevho, Z. Ferreira, A. Ayeleso, Potential role of sulfur-containing antioxidant systems in highly oxidative environments, Molecules 19 (12) (2014) 19376–19389, https://doi.org/10.3390/molecules191219376.
[116] M. Rezvanain, N. Ahmad, M.C.I. Mohd Amin, S.F. Ng, Optimization, characterization, and in vitro assessment of alginate-pectin ionic cross-linked hydrogel film for wound dressing applications, Int. J. Biol. Macromol. 97 (2017) 131–140, https://doi.org/10.1016/j.ijbiomac.2016.12.079.
[117] A.S. Soubhagya, A. Moorthi, M. Prabaharan, Preparation and characterization of chitosan/pectin/ZnO porous films for wound healing, Int. J. Biol. Macromol. 157 (2020) 135–145, https://doi.org/10.1016/j.ijbiomac.2020.04.156.
[118] K. Song, et al., Preparation of pectin-chitosan hydrogels based on bioadhesive-design micelle to prompt bacterial infection wound healing, Carbohydr. Polym. 300 (June) (2022) 2023, https://doi.org/10.1016/j.carbpol.2022.120272.

[119] W. Qiu, et al., Nanofibers reinforced injectable hydrogel with self-healing, antibacterial, and hemostatic properties for chronic wound healing, J. Colloid Interface Sci. 596 (2021) 312–323, https://doi.org/10.1016/j.jcis.2021.02.107.
[120] N. Hasan, J. Cao, J. Lee, H. Kim, J.W. Yoo, Development of clindamycin-loaded alginate/pectin/hyaluronic acid composite hydrogel film for the treatment of MRSA-infected wounds, J. Pharm. Investig. 51 (5) (2021) 597–610, https://doi.org/10.1007/s40005-021-00541-z.
[121] M. Brenner, C. Hilliard, G. Peel, G. Crispino, R. Geraghty, G. O'Callaghan, Management of pediatric skin-graft donor sites: A randomized controlled trial of three wound care products, J. Burn Care Res. 36 (1) (2015) 159–166, https://doi.org/10.1097/BCR.0000000000000161.
[122] J.C. Dumville, S.J. Keogh, N. Stubbs, R.M. Walker, Alginate dressings for treating pressure ulcers, Cochrane Database Syst. Rev. 8 (2014) 2014, https://doi.org/10.1002/14651858.CD011277.
[123] M.P. Sintler, A. Mahmood, S.R.G. Smith, M.H. Simms, R.K. Vohra, Randomized trial comparing quixil surgical sealant with kaltostat hemostatic dressing to control suture line bleeding after carotid endarterectomy with ePTFE patch reconstruction, World J. Surg. 29 (10) (2005) 1259–1262, https://doi.org/10.1007/s00268-005-7863-4.
[124] S. Saghazadeh, et al., Drug delivery systems and materials for wound healing applications, Adv. Drug Deliv. Rev. 127 (2018) 138–166, https://doi.org/10.1016/j.addr.2018.04.008.
[125] H. Singh, et al., Curcumin in decellularized goat small intestine submucosa for wound healing and skin tissue engineering, J. Biomed. Mater. Res. - Part B Appl. Biomater. 110 (1) (2022) 210–219, https://doi.org/10.1002/jbm.b.34903.
[126] M. Zakerikhoob, S. Abbasi, G. Yousefi, M. Mokhtari, M.S. Noorbakhsh, Curcumin-incorporated crosslinked sodium alginate-g-poly (N-isopropyl acrylamide) thermo-responsive hydrogel as an in-situ forming injectable dressing for wound healing: In vitro characterization and in vivo evaluation, Carbohydr. Polym. 271 (June) (2021), https://doi.org/10.1016/j.carbpol.2021.118434.
[127] D. Archana, B.K. Singh, J. Dutta, P.K. Dutta, Chitosan-PVP-nano silver oxide wound dressing: In vitro and in vivo evaluation, Int. J. Biol. Macromol. 73 (1) (2015) 49–57, https://doi.org/10.1016/j.ijbiomac.2014.10.055.
[128] S.G. Jin, et al., In vivo wound-healing effects of novel benzalkonium chloride-loaded hydrocolloid wound dressing, Drug Dev. Res. 76 (3) (2015) 157–165, https://doi.org/10.1002/ddr.21253.
[129] R. Portela, C.R. Leal, P.L. Almeida, R.G. Sobral, Bacterial cellulose: a versatile biopolymer for wound dressing applications, J. Microbial. Biotechnol. 12 (4) (2019) 586–610, https://doi.org/10.1111/1751-7915.13392.
[130] J.P. Sundberg, L.B. Nanney, P. Fleckman, L.E. King, *Skin and Adnexa*, First Edit. Elsevier Inc., 2012.
[131] P.M. Treuting, S.M. Dintzis, K.S. Montine, *Comparative Anatomy And Histology: A Mouse, Rat, And Human Atlas Second Edition*. 2018.
[132] L. Dunn, H.C.G. Prosser, J.T.M. Tan, L.Z. Vanags, M.K.C. Ng, C.A. Bursill, Murine model of wound healing, J. Vis. Exp. 2013 (75) (2013) 1–6, https://doi.org/10.3791/50265.
[133] P.H. Wang, B.S. Huang, H.C. Horng, C.C. Yeh, Y.J. Chen, Wound healing, J. Chin. Med. Assoc. 81 (2) (2018) 94–101, https://doi.org/10.1016/j.jcma.2017.11.002.
[134] A. Guerra, J. Belinha, R.N. Jorge, Modelling skin wound healing angiogenesis: A review, J. Theor. Biol. 459 (2018) 1–17, https://doi.org/10.1016/j.jtbi.2018.09.020.
[135] I. Pastar, et al., Epithelialization in wound healing: A comprehensive review, Adv. Wound Care 3 (7) (2014) 445–464, https://doi.org/10.1089/wound.2013.0473.
[136] J.G. Powers, C. Higham, K. Broussard, T.J. Phillips, Wound healing and treating wounds Chronic wound care and management, J. Am. Acad. Dermatol. 74 (4) (2016) 607–625, https://doi.org/10.1016/j.jaad.2015.08.070.
[137] T. Velnar, T. Bailey, V. Smrkolj, The wound healing process: An overview of the cellular and molecular mechanisms, J. Int. Med. Res. 37 (5) (2009) 1528–1542, https://doi.org/10.1177/147323000903700531.
[138] B.G. Ongarora, Recent technological advances in the management of chronic wounds: A literature review, Health Sci. Rep. 5 (3) (2022) 1–10, https://doi.org/10.1002/hsr2.641.
[139] M.A. Alsakhawy, D.A. Abdelmonsif, M. Haroun, S.A. Sabra, Naringin-loaded Arabic gum/pectin hydrogel as a potential wound healing material, Int. J. Biol. Macromol. 222 (June) (2022) 701–714, https://doi.org/10.1016/j.ijbiomac.2022.09.200.
[140] N.N. Nordin, N.K. Aziz, I. Naharudin, N.K. Anuar, Effects of drug-free pectin hydrogel films on thermal burn wounds in streptozotocin-induced diabetic rats, Polymers 14 (14) (2022) 2873, https://doi.org/10.3390/polym14142873.
[141] M. Zare-Gachi, et al., Improving anti-hemolytic, antibacterial and wound healing properties of alginate fibrous wound dressings by exchanging counter-cation for infected full-thickness skin wounds, Mater. Sci. Eng. C 107 (2020) 110321, https://doi.org/10.1016/j.msec.2019.110321.
[142] M. Awale, X. Jin, J.L. Reymond, Stereoselective virtual screening of the ZINC database using atom pair 3D-fingerprints, J. Cheminf. 7 (1) (2015) 1–15, https://doi.org/10.1186/s13321-014-0051-5.
[143] M. Saghi, A. Arastehnodeh, Optimization of Enaminone structures and investigation of substituent effects on molecular stability using HF and DFT soft computational methods, Int. J. New Chem. 5 (2) (2018) 65–75.
[144] B.R. Brooks, et al., CHARMM: The biomolecular simulation program, J. Comput. Chem. 30 (10) (2009) 1545–1614, https://doi.org/10.1002/jcc.21287.
[145] S. Jo, K.C. Song, H. Desaire, A.D. MacKerell, W. Im, Glycan reader: Automated sugar identification and simulation preparation for carbohydrates and glycoproteins, J. Comput. Chem. 32 (14) (2011) 3135–3141, https://doi.org/10.1002/jcc.21886.
[146] W.L. DeLano, Pymol: An open-source molecular graphics tool, CCP4 Newsletter on Protein Crystallogr. 40 (2002) 82–92.
[147] D. Beckedahl, E.O. Obaga, D.A. Uken, A. Sergi, M. Ferrario, On the configurational temperature Nosè-Hoover thermostat, Physica A 461 (2016) 19–35, https://doi.org/10.1016/j.physa.2016.05.008.
[148] D. Quigley, M.I.J. Probert, Langevin dynamics in constant pressure extended systems, J. Chem. Phys. 120 (24) (2004) 11432–11441, https://doi.org/10.1063/1.1755657.
[149] B.A. Luty, M.E. Davis, I.G. Tironi, W.F. Van Gunsteren, A comparison of particle-particle, particle-mesh and ewald methods for calculating electrostatic interactions in periodic molecular systems, Mol. Simul. 14 (1) (1994) 11–20, https://doi.org/10.1080/08927029408022004.
[150] H.C. Andersen, Rattle: A 'velocity' version of the shake algorithm for molecular dynamics calculations, J. Comput. Phys. 52 (1) (1983) 24–34, https://doi.org/10.1016/0021-9991(83)90014-1.
[151] O. Guvench *et al.*, "CHARMM Additive All-Atom Force Field for Carbohydrate Derivatives and Its Utility in Polysaccharide and Carbohydrate À Protein Modeling," pp. 3162–3180, 2011.
[152] J.C. Phillips *et al.*, "Scalable Molecular Dynamics with NAMD," 2005, doi: 10.1002/jcc.20289.
[153] J.C. Suérez, S. Miguel, P. Pinilla, F. López, Molecular dynamics simulation of polymer-metal bonds, J. Adhes. Sci. Technol. 22 (13) (2008) 1387–1400, https://doi.org/10.1163/156856108X305732.
[154] H. Robson, Verified syntheses of zeolitic materials, Verified Syntheses Zeolitic Mater. (2001), https://doi.org/10.1016/b978-0-444-50703-7.x5094-7.
[155] D.F. Swinehart, The Beer-Lambert law, J. Chem. Educ. 39 (7) (1962) 333–335, https://doi.org/10.1021/ed039p333.
[156] D. Caccavo, An overview on the mathematical modeling of hydrogels' behavior for drug delivery systems, Int. J. Pharm. 560 (December 2018) (2019) 175–190, https://doi.org/10.1016/j.ijpharm.2019.01.076.
[157] P.N. Dave, P.M. Macwan, B. Kamaliya, Biodegradable Gg-cl-poly(NIPAm-co-AA)/-o-MWCNT based hydrogel for combined drug delivery system of metformin and sodium diclofenac: in vitro studies, RSC Adv. 13 (33) (2023) 22875–22885, https://doi.org/10.1039/d3ra04728h.
[158] T. Thanyacharoen, P. Chuysinuan, S. Techasakul, P. Nooeaid, S. Ummartyotin, Development of a gallic acid-loaded chitosan and polyvinyl alcohol hydrogel composite: Release characteristics and antioxidant activity, Int. J. Biol. Macromol. 107 (PartA) (2018) 363–370, https://doi.org/10.1016/j.ijbiomac.2017.09.002.
[159] D. Wójcik-Pastuszka, J. Krzak, P. Prządka, M. Twarda, B. Osiński, W. Musiał, Release of bupivacaine from artificial ligament implants modified with the silica coating, Ceram. Int. 49 (2) (2023) 2852–2859, https://doi.org/10.1016/j.ceramint.2022.09.267.
[160] P. Zahedi, I. Rezaeian, S.O. Ranaei-Siadat, S.H. Jafari, P. Supaphol, A review on wound dressings with an emphasis on electrospun nanofibrous polymeric bandages, Polym. Adv. Technol. 21 (2) (2010) 77–95, https://doi.org/10.1002/pat.1625.
[161] M. Uzun, S.C. Anand, T. Shah, *In vitro* characterisation and evaluation of different types of wound dressing materials, J. Biomed. Eng. Technol. 1 (1) (2013) 1–7, https://doi.org/10.12691/jbet-1-1-1.
[162] ASTM, "ASTM D522: Standard Test Methods for Mandrel Bend Test of Attached Organic Coatings," 2001.
[163] British Standards Institution, "BS EN 12127: Determination of mass per unit area using small samples," 1998.
[164] British Standards Institution, "Textiles — Test methods for nonwovens Part 2. Determination of thickness," 2008.
[165] British Standards Institution, "BS EN 13726-1: Test methods for primary wound dressings. Part 1: aspects of absorbency.," 2002.
[166] D. Parsons, P.G. Bowler, V. Myles, S. Jones, Silver antimicrobial dressings in wound management: A comparison of antibacterial, physical, and chemical characteristics, Wounds 17 (8) (2005) 222–232.
[167] Bsbe, "Test methods for primary wound dressings. Part 1: aspects of absorbency.," *British Standard Institute*, p. Fluid handling capacity BSBE 13726-1, 2002.
[168] C. Cao, et al., Biodegradable hydrogel with thermo-response and hemostatic effect for photothermal enhanced anti-infective therapy, Nano Today 39 (2021) 101165, https://doi.org/10.1016/j.nantod.2021.101165.
[169] Z. Özbaş, G. Torkay, A. Bal-Öztürk, B. Özkahraman, Preparation of quercetin incorporated photocrosslinkable methacrylated gelatin/methacrylated kappa-carrageenan antioxidant hydrogel wound dressings, Chem. Pap. 76 (12) (2022) 7597–7606, https://doi.org/10.1007/s11696-022-02426-3.
[170] S. Tyeb, N. Kumar, A. Kumar, V. Verma, Flexible agar-sericin hydrogel film dressing for chronic wounds, Carbohydr. Polym. 200 (January) (2018) 572–582, https://doi.org/10.1016/j.carbpol.2018.08.030.
[171] A. Mirzaei-Mohkam, F. Garavand, D. Dehnad, J. Keramat, A. Nasirpour, Optimisation, antioxidant attributes, stability and release behaviour of carboxymethyl cellulose films incorporated with nanoencapsulated vitamin E, Prog. Org. Coat. 134 (April) (2019) 333–341, https://doi.org/10.1016/j.porgcoat.2019.05.026.
[172] T.L. Schenck, et al., A full skin defect model to evaluate vascularization of biomaterials in vivo, J. Vis. Exp. 90 (2010) 51428.
[173] G. Giusto, C. Vercelli, F. Comino, V. Caramello, M. Tursi, M. Gandini, A new, easy-to-make pectin-honey hydrogel enhances wound healing in rats, BMC Complement. Altern. Med. 17 (1) (2017) 1–7, https://doi.org/10.1186/s12906-017-1769-1.